Atomic scale simulations for the diffusion-assisted crossing of dislocation anchored by vacancy clusters

Marie Landeiro Dos Reis, Laurent Proville,* and Mihai-Cosmin Marinica
DEN-Service de Recherches de Métallurgie Physique, CEA, Université Paris-Saclay, F-91191, Gif-sur-Yvette, France

Maxime Sauzay
DEN-Service de Recherches de Métallurgie Appliquée, CEA, Université Paris-Saclay, F-91191, Gif-sur-Yvette, France

(Received 19 February 2020; revised 13 May 2020; accepted 18 September 2020; published 2 October 2020)

Nanosize vacancy clusters, characterized in metals after plastic deformation, irradiation or specific heat treatments are suspected to participate in materials hardening through their interactions with mobile dislocations. Our numerical simulations made from combining three different simulation techniques, i.e., molecular statics, kinetic Monte Carlo and elastic line models allow us to compute the dislocations velocity in realistic conditions of applied shear stress, temperature, concentration, and size of the vacancy clusters, in face–centered-cubic aluminium. We show that the clusters behave as sources of vacancies that follow a reaction path along the dislocation line, which is recognized as a pipe diffusion process. The accumulation of vacancies in the dislocation stacking fault ribbon yields jogs that participate in the dislocation climb. Both vacancy leaks from clusters and climb of dislocation segments contribute to the dislocation crossing, which remains thermally activated. We integrated the ensemble of the thermally activated processes: Diffusion, emission, absorption processes, as well as dislocation-cluster crossing, into the same simulation allowing us to predict the dislocation mobility in good agreement with experimental deformation tests.

DOI: 10.1103/PhysRevMaterials.4.103603

I. INTRODUCTION

Vacancy clusters were identified experimentally in various strained metals [1–7], high-purity quenched metals [1,8] or irradiated metals [1,9,10] where their origin is much better understood [11]. Different experimental studies [12–15] revealed that the vacancy clusters reduce in size spontaneously in course of time observation thereby confirming their instability. Such an evaporation process due to the emission of single vacancy from clusters accelerates when the clusters are in contact with a dislocation. Vacancy diffusion along dislocation cores can be several orders of magnitude faster than the one observed in the bulk due to the local lattice distortion generated by the elastic strain field of the dislocations [16–21] that induced a one-dimensional diffusion process, known as pipe diffusion [12–15,22–24].

Modeling the interaction between vacancy clusters and dislocations is by nature complex as the long time diffusion process of vacancies is entangled with the atomic details of the dislocation core. In order to develop a model accounting for the atom interactions as well as for diffusion processes, we have nested different simulations. First, we employed molecular statics (MS) simulation techniques to determine the energy landscape of a crystal including vacancies, dislocation, and vacancy clusters, considering the eventual formation of jogs. We chose to study the archetypical case of face-centered-cubic (fcc) aluminium because a quantity of experimental observations is available in the literature [12,13,15,25].

Then we introduced a lattice kinetic Monte Carlo model (KMC) [26] that reproduces at the atomic scale the thermally activated processes identified through MS: (i) the vacancy emission (absorption) from clusters and jogs; (ii) the vacancy migration in bulk and in the stacking fault ribbon of the dislocation; (iii) the dislocation crossing vacancy clusters. In such a model, the vacancies and the dislocation segments are treated as interacting objects and the dislocation is represented through an elastic line model (ELM) [27]. The main achievement of the present work is the construction of a combined KMC-ELM model, which the sole parameters are determined from MS calculations.

We show the primary role of the pipe diffusion in the unpinning of dislocations, as it contributes to a decrease of the cluster size through vacancy release [12–15] and to the dislocation climb mechanism [28–35]. We determined the average waiting time the dislocation is anchored by the clusters for different applied shear stresses, temperatures, and vacancy cluster sizes. The KMC-ELM model allowed us to produce simulations of the motion of a dislocation in realistic conditions of stress and temperature in a three-dimensional random distribution of vacancy clusters, for concentrations identified in experiments [1–7]. Our predictions for dislocation velocities are of the order of μm/s under an applied stress of several MPa, which agrees well with tensile deformation experiments in high purity cubic aluminium at room temperature [36,37].

The MS simulations are presented in Sec. II. In Sec. III, the KMC-ELM simulation is presented for the dislocation

*laurent.proville@cea.fr

TABLE I. Comparison between fundamental properties of Al computed with EAM potential [39,40] and experiments. a_0 is the lattice parameter, C_{11} and C_{12} are the elastic constants, d_{ed} is the dissociation distance for the edge dislocation, E_f^{pc} and E_m^{pc} are, respectively, the formation and migration energy in a perfect crystal for a vacancy.

	EAM	Experiments
a_0 (Å)	4.032	4.0315 [41]
C_{11} (GPa)	118	105.6-112.9 [42]
C_{12} (GPa)	62	60.41-66.5 [42]
d_{ed} (Å)	15.97	5.5-40 [43]
E_f^{pc} (eV)	0.69	0.66 [44–47]; 0.73 ± 0.03 [48]
		0.69 ± 0.03 [49]
E_m^{pc} (eV)	0.61	0.61 [45];0.75 ± 0.08 [48];0.62 [47]

interaction with a single cluster, while Sec. IV concerns the dislocation motion through a random distribution of clusters. Our results are discussed in Sec. V.

II. MOLECULAR STATIC SIMULATIONS

A. Diffusion around vacancy clusters

We have computed the energy barriers for the vacancy diffusion in two different situations: (i) in the vicinity of an isolated void and (ii) at the interface between a vacancy cluster and an edge dislocation.

To treat the case of an isolated void, we built a simulation cell containing 66 546 atoms where we introduced a cavity by removing the atoms contained in a sphere as described in Ref. [38]. The interatomic potential we used for our atomic scale computations is the embedded atom method (EAM) potential proposed by Liu *et al.* [39,40], which provides a good description of vacancy formation energy, E_f^{pc}, and migration barrier, E_m^{pc} (see Table I).

In order to determine the relaxed atomic positions in our simulation cell a Langevin dynamics [50] was employed. During the simulation, the position $\vec{r}_i$ and the velocity $\vec{v}_i$ of the atom i were determined through a simple first order Runge-Kutta algorithm [51,52]: $\vec{r}_i = \vec{r}_i + \vec{v}_i \delta t$ and $\vec{v}_i = \vec{v}_i + \vec{a}_i \delta t$, where $\vec{a}_i = \frac{\vec{f}_i}{m_i} - \lambda \vec{v}_i$ is the usual Newton acceleration $\frac{\vec{f}_i}{m_i}$ to which the Langevin friction term $-\lambda \vec{v}_i$ was added to damp the system dynamics [38]. The step δt of our computations was set to 0.1 fs and the friction coefficient λ to 1000 THz. We have verified that the potential reproduces well the fundamental properties of importance for our study (see Table I). Although more recent potentials were developed, the potential used here has proved to be robust in different works [53,54] with a relatively low computational load. That is a strong asset to our study where numerous computations involving large simulation cells to capture physics of dislocations and cavities are required.

In the case of an isolated cavity, we used periodic boundary conditions in the three directions of the space. The simulation cell is constructed by repeating in three directions a unit cell made from the three vectors: $a_0[110]/2$ along x, $a_0[\bar{1}12]/2$ along y and $a_0[1\bar{1}1]$ along z. This elementary cell contains six atoms when the perfect fcc crystal symmetry is applied.

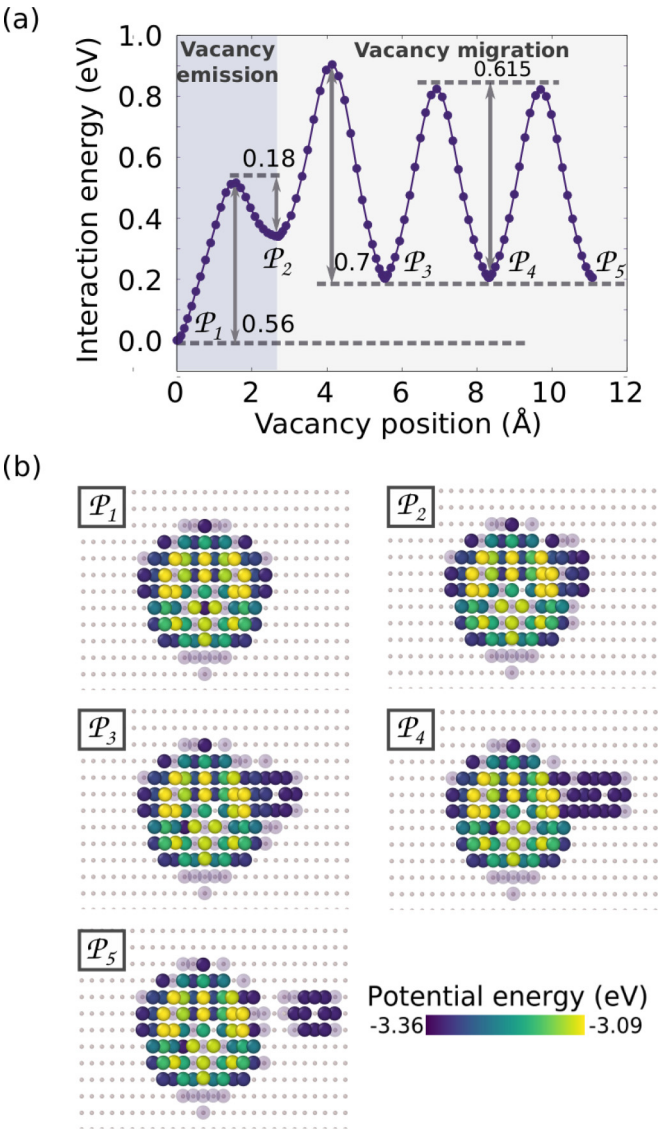

FIG. 1. (a) Energy landscape of a vacancy in the vicinity of a cavity of radius r = 6 Å along [110] direction, obtained by NEB [55–57]. We quoted by the letters $\mathcal{P}_i$ the minima of the energy landscape. (b) Snapshot of atomic configurations corresponding to the minima $\mathcal{P}_i$. The color, the size, and the transparency of the atoms are chosen according to their potential energy (see the legend for colors). The atoms in situation close from the perfect crystal symmetry appear like spots.

Once properly relaxed, the simulation cell containing a cavity, we determined the minimum energy path (MEP) for the emission process of a single vacancy using the nudged elastic band (NEB) method [55–57] (see the blue area corresponding to the vacancy emission in Fig. 1(a)). The force relaxation criterion was fixed to 10^{-4} eV/Å and the NEB constant spring force was fixed to 5 eV/Å. The computations were realized with 25 NEB replica. The initial path imposed to an atom at the edge of the vacancy cluster corresponds to a displacement along the [110] direction with amplitude of $b = \frac{a_0}{\sqrt{2}}$. To determine the migration energy barrier further in the bulk, i.e. at larger distance from the cluster, we performed a different NEB computation starting from the final state

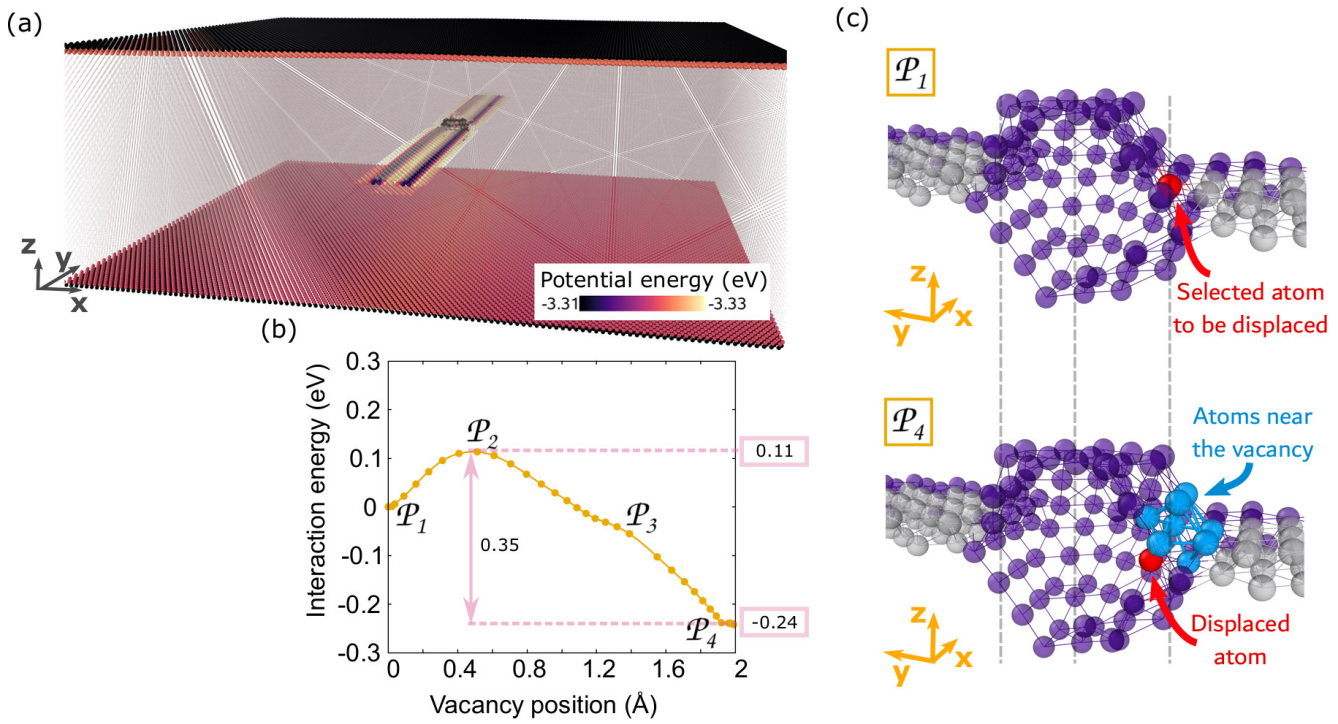

FIG. 2. (a) 3D view of the simulation cell. The unit cell vectors are $a_0[110]/2$ in x, $a_0[\bar{1}12]/2$ in y and $a_0[1\bar{1}1]$ in z. The color, the size, and the transparency of the atoms are chosen according to their potential energy as in Fig. 1. The Shockley partials of the edge dislocation as well as the vacancy cluster and the surfaces appear spontaneously within such a color code. (b) Energy landscape for the emission of a vacancy from an isolated cavity toward the dislocation core obtained by NEB. We quoted by the letters $\mathcal{P}_i$ some key points of the energy path. (c) Initial $\mathcal{P}_1$ and final $\mathcal{P}_4$ atomic configurations that correspond to the energy path shown in (b). A crystal cut is made such that only one half of the dislocation and the cavity are visible. The atoms that have a first neighbor cell with a perfect fcc symmetry are not shown. The color code is (i) in gray the atoms of the dislocation stacking fault; (ii) in dark blue the neighbors of the cavity and those of the Shockley partial dislocations; (iii) in red the selected atom that moves to yield the first vacancy jump; (iv) in light blue the first neighbors of the vacancy.

of the previous one, i.e., configuration $\mathcal{P}_2$ in Fig. 1(a). The final state corresponds then to a jump of the vacancy in the direction [110] at distance b, configuration $\mathcal{P}_2$ in Fig. 1(b). It corresponds to a jump of the next neighbor atom in the [110] direction in the opposite direction. We repeated such a computation two more times such that the vacancy reaches a distance of $4b$ from the voids. The quasispherical symmetry of clusters allowed us to limit our computation to the unique path shown in Fig. 1(b).

Once the vacancy reaches the configuration $\mathcal{P}_3$ [Figs. 1(a) and 1(b)], it is more favorable for the vacancy to go further in the bulk, toward configuration $\mathcal{P}_4$ and then $\mathcal{P}_5$ than to come back. After only two jumps from the cavity, the vacancy migration barrier reaches a value very closed to E_m^{pc} (see Table I). Hence, the far elastic field around the cavity has a negligible influence on the vacancy migration barrier. However, the potential energy landscape of a vacancy is strongly modified in the close vicinity of the cluster. We have repeated the very same computations but applying an hydrostatic stress to the simulation cell and we noticed that the vacancy energy barriers do not depend significantly on the external stress below a stress level of several GPa. It is also interesting to notice that at configuration $\mathcal{P}_1$ in Figs. 1(a) and 1(b) the vacancy is more stable than in the bulk (at configuration $\mathcal{P}_5$). It indicates the stability of the nanovoids in our computation, in absence of different sinks as surfaces [25] or dislocations [13].

We consider now the energy landscape of the vacancy at the interface between a cavity and an edge dislocation in which the Burgers vector is oriented along [110] with a norm $b = \frac{a_0}{\sqrt{2}}$. As detailed in Refs. [27,38,58], we built a simulation cell of 750 000 atoms containing an edge dislocation, free surfaces and a vacancy cluster (see Fig. 2(a)). We applied a shear stress to the free surfaces, slightly larger than the Peierls stress (i.e., a few MPa in the present case) such that the dislocation glides up to encounter the cluster since the system is driven by the Langevin dynamics. Then we removed the applied stress and pursued the energy relaxation of the system to reach the force relaxation criterion aforementioned. The notations are the same as in the previous simulations. We determined the MEP for the vacancy emission process using the same NEB method but with 35 NEB replica [see Fig. 2(b)]. The atom selected to move toward the vacancy cluster is colored in red in the atomic configuration $\mathcal{P}_1$ in Fig. 2(c). The initial NEB path we imposed to this atom is (0.8 Å; 1.12 Å; −2.28 Å) in the repair of the simulation cell. Such a path is equivalent to a jump of a distance b in the [110] direction, examined previously in the case of the isolated cluster. However, in the present case, we have selected a [110] direction such that the atom-vacancy motion proceeds

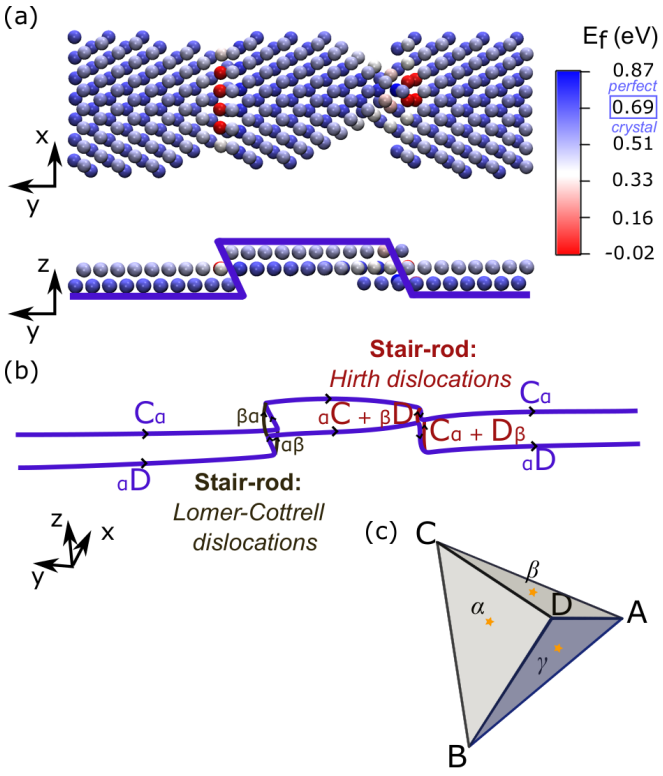

FIG. 3. (a) Jogged dislocation in molecular static simulations. The unit vectors are same as in Fig. 2. Each atom is colored according to the formation energy of the vacancy that could be superseded to it. (b) Schematic representation for a jogged dislocation. The Burgers vectors of the different dislocations are indicated. We denoted by $\alpha\mathcal{D}$ and $\mathcal{C}\alpha$, the Burgers vectors of the Shockley partial dislocations, which corresponds to a vector ($\frac{a_0}{6}\langle 112\rangle$). The Burgers vectors of the Lomer-Cottrell stair-rod dislocations are $\alpha\beta$ and $\beta\alpha$, which corresponds to a vector ($\frac{a_0}{3}\langle 001\rangle$). The Burgers vectors of the Hirth stair-rod dislocations are $\mathcal{C}\alpha + \mathcal{D}\beta$, $\alpha\mathcal{C} + \beta\mathcal{D}$, which corresponds to a vector ($\frac{a_0}{6}\langle 110\rangle$). (c) Thompson tetrahedron [59] showing the different dislocation Burgers vectors.

inside the dislocation core. We selected the path that leads to the more stable position. We noticed that the energy barrier for the emission process, of 0.11 eV [see $\mathcal{P}_2$ in Fig. 2(b)] is by far much lower than for an isolated cluster [Fig. 1(a)]. Furthermore, the final state of the system, quoted by the letter $\mathcal{P}_4$ in Fig. 2(b) corresponds to a stable configuration with an energy smaller than the initial one, quoted by $\mathcal{P}_1$. Hence, the emission of a vacancy from a cluster is favorable in presence of the dislocation and the cluster becomes unstable once it is in contact with the dislocation. Such a property will be further discussed in the next section.

B. Diffusion around dislocation jogs

Vacancies interact with the dislocation jogs in a peculiar manner [60] so we examined such an interaction in a simulation cell with 177 650 atoms, containing a jogged dislocation [see Fig. 3(a)]. The jogs characterized by their height h_{jogs} and the distance d_{jogs} between each other were introduced by selecting a portion of the dislocation line of length d_{jogs} where, instead of removing the atoms of the entire half (110) plane, as done to introduce a perfect straight dislocation [58] we only removed the atoms above h_{jogs}. For the purpose of the present study we examined only the jogs with height $h_{\text{jogs}} = u_z$, where $u_z = a_0/\sqrt{3}$ corresponds to the inter-reticular distance perpendicular to the glide plane, i.e., in the z[1$\bar{1}$1] direction. Higher jogs, with $h_{\text{jogs}} > u_z$, are energetically costlier according to our computations. The force criterion was fixed to 1.10^{-4} eV/Å.

In Fig. 3(a) one notes that stair-rod dislocations are formed at the position of the jogs and we distinguish acute and obtuse jogs as in the seminal work of Thomson [59]. On the acute jog, the Shockley partial dislocations are stair-rods of type Lomer-Cottrell, with a Burgers vectors $\frac{a_0}{3}\langle 001\rangle$, quoted $\alpha\beta$ or $\beta\alpha$ according to the standard Thomson tetrahedron [59] [see Figs. 3(b) and 3(c)]. On the obtuse jog, the Shockley partial dislocations are stair-rods of type Hirth, with a Burgers vectors $\frac{a_0}{6}\langle 110\rangle$, quoted $\mathcal{C}\alpha + \mathcal{D}\beta$ or $\alpha\mathcal{C} + \beta\mathcal{D}$.

We computed the formation energy, E_f, for a vacancy that would be introduced inside the dislocation core:

$$E_f = E - (N_{\text{at}} - 1)\frac{E_0}{N_{\text{at}}}, \tag{1}$$

where E_0 is the total potential energy of the simulation cell containing a perfect crystal with a total of N_{at} atoms, and E is the potential energy of the same simulation cell but where a vacancy has been introduced by removing only one atom. The formation energy depends on the position of the atom removed, as shown by the color code used in Fig. 3(a). The formation energy of the vacancy is close to zero inside the stair-rod dislocations [see the atoms colored in red in Fig. 3(a)]. The stair-rod dislocations are said to be perfect sinks for vacancies [28].

We computed the energy barrier for the emission of a vacancy from a dislocation jog in two different situations: (i) Config. 1 in Fig. 4(a), an atom from the bulk is displaced inside the core of a Lomer-Cottrell dislocation (it corresponds to the emission of a vacancy from a stair-rod dislocation core toward the bulk); (ii) Config. 2 in Fig. 4(a), an atom from a Shockley partial dislocation is displaced inside the core of a Hirth dislocation (it corresponds to the emission of a vacancy from a stair-rod dislocation core toward a Shockley partial dislocation core). To determine the energy barriers corresponding to the emission processes we employed the NEB method as described previously, with 40 replicas [see Fig. 4(b)]. The MEP corresponding to Config. 1 in Fig. 4(a) was computed with an initial NEB path given by the vector (−1.4 Å; −2.5 Å; 0 Å) while for Config. 2 the initial NEB path was given by the vector (−0.61 Å; 1.17 Å; −2.4 Å) in the simulation cell repair. In Config. 1 we obtained an energy barrier of 0.98 eV [see Fig. 4(b)] much higher than in Config. 2, which is 0.76 eV [see Fig. 4(b)]. It is interesting to notice that the vacancy emission from a cluster, either isolated or in contact with a dislocation (see Sec. II A) corresponds to lower energy barriers, which thus indicates that the main vacancy sources are definitely the vacancy clusters.

C. Vacancy diffusion in the vicinity of a dislocation

The potential energy landscape of a vacancy was computed as a function of the distance between vacancy and

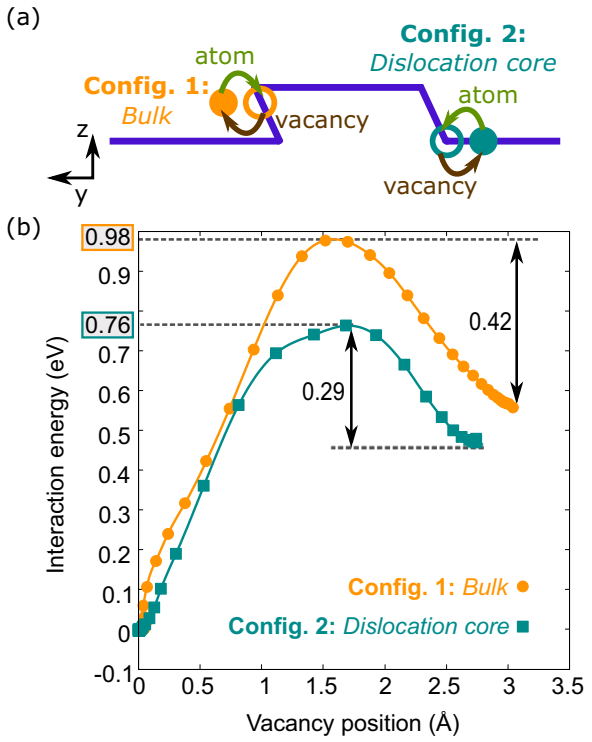

FIG. 4. (a) Schematic representation of two vacancy emission processes from the dislocation jogs: Config. 1: A vacancy is emitted from a Lomer-Cottrell stair-rod dislocation toward the bulk, Config. 2: A vacancy is emitted from a Hirth stair-rod dislocation toward a Shockley partial dislocation core. (b) Energy barrier for the two emission processes: Config. 1 (yellow circles) and Config. 2 (green squares).

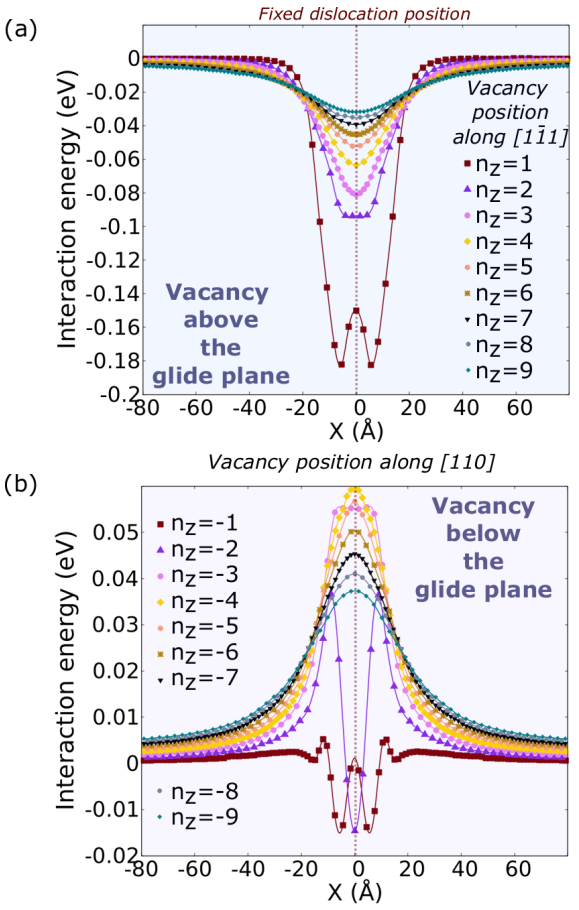

FIG. 5. Interaction energy between dislocation and vacancy computed from MS simulations: (a) vacancy above the glide plane ($n_Z > 0$), (b) vacancy below the glide plane ($n_Z < 0$). n_Z is the number of (1$\bar{1}$1) crystal plane between the dislocation glide plane and the vacancy.

dislocation along the two directions $x[110]$ and $z[1\bar{1}1]$. We built a simulation cell containing 177 000 atoms with an edge type dislocation, two free surfaces and a single vacancy [38,58]. The force criterion was fixed to 10^{-4}eV/Å. We denoted by x_v and x_{dislo} the positions of the vacancy and the dislocation along $x[110]$. x_{dislo} is determined thanks to the difference between the potential energy, e_i^p, of atom i situated at x_i and the cohesive energy of the perfect crystal, E_{coh}, through the barycenter formula [38]. We denoted $X = (x_v - x_{\text{dislo}})$ the distance between the vacancy and the dislocation. The interaction energy between the vacancy and the dislocation is defined by $E_{\text{int}} = E - E_\infty$, where E is the energy of our simulation cell and E_∞ is the energy of the same system but when the dislocation and the vacancy are separated by a large distance. For a vacancy situated above the glide plane the interaction energy is attractive and its maximum amplitude decreases when the distance to the glide plane increases [see Fig. 5(a)].

Let n_Z be the number of crystal planes between the dislocation glide plane and the vacancy position in $z[1\bar{1}1]$ direction. n_Z is positive when the vacancy is above the glide plane and negative in the other case. E_{int} remains significant at least up to the fourth plane above the glide plane. Two minima are well distinguished and correspond to the dislocation partials interaction with the vacancy when $n_Z = 1$. When the vacancy distance to the dislocation glide plane is large enough, only one hump is observed in E_{int}. For a vacancy below the glide plane, the interaction is attractive near the dislocation core [see Fig. 5(b)]. However, it becomes more and more repulsive when $|n_Z|$ increases, up to reach a maximum at $n_Z = -4$. Below the maximum amplitude of E_{int} decreases as $|n_Z|$ increases and it remains repulsive.

By contrast to the predictions made from standard elastic theory [54], the interaction energy is not symmetric with respect to mirror inversion through the glide plane. The same discrepancy has been noticed by different authors in different crystals [29,54]. In Appendix A, we have reported the comparison between the standard elastic theory and our results from MS simulations. These results correspond merely to the effect of the complex elastic field of a straight dislocation on the nearby vacancy (see Fig. 5). Indeed, the elastic field of the dislocation yields a local deformation of the atomic-network and such a deformation field interacts with the elastic deformation field of the vacancy. The energy variation against the distance between the dislocation and the vacancy corresponds to the interaction energy. The dislocation-vacancy interaction is modified in the presence of a vacancy cluster. In order to quantify such an effect we realized the same computations as in Figs. 5(a) and 5(a) but this time, in a system that contains a dislocation anchored on a vacancy cluster. For such

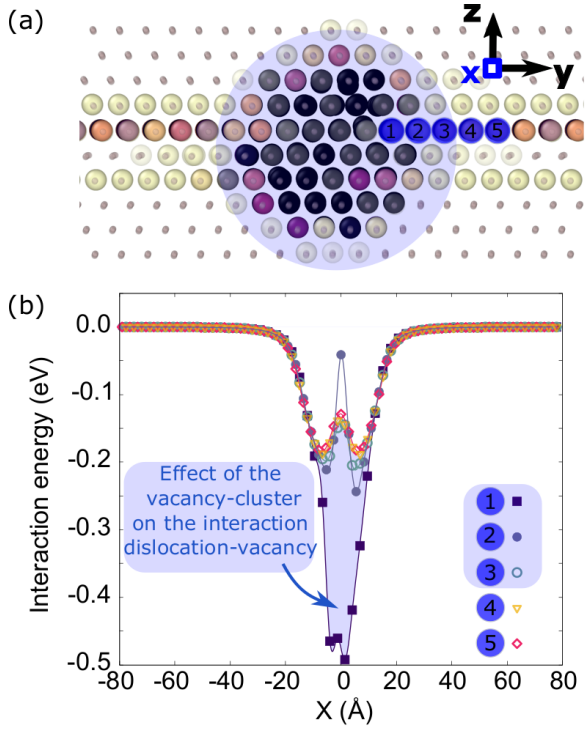

FIG. 6. (a) Magnification of the atomic configuration near the pinning point. We have highlighted by blue circles quoted from 1 to 5, the atomic rows oriented in x[110] along which we have computed the interaction energy dislocation-vacancy reported in (b). (b) Interaction energy computed from MS simulations between the dislocation and the vacancy in the crystal plane defined by $n_Z = 1$. The row quoted 1 corresponds to the nearest row from the cavity. We shaded in blue the difference between the curves corresponding to row 1 and row 5 in order to highlight the effect of cavity.

simulations we used the same conditions as those described for Fig. 2. We reported in Fig. 6 the variation of the interaction energy along different crystal rows oriented in the x[110] direction in the plane $n_Z = 1$, i.e., the plane where the vacancy has the maximum interaction energy, as shown in Fig. 5(a). When the vacancy is situated in a row far enough from the cavity, say at five interatomic distances from the periphery of the cavity, i.e., the row labeled with number 5 in Fig. 6, the dislocation-vacancy energy landscape is very similar to the one found in Fig. 5(a), where no cavity was present in the simulation cell. The effect of the cavity is then negligible. When one considers a row situated in the vicinity of the cavity, i.e., row number 1 in Fig. 6, then the profile of the interaction energy is much deeper. It means that the interface between the dislocation and the cavity is much more attractive than other positions along the dislocation or other positions at the surface of the cavity. According to Fig. 6, beyond three interatomic distances in $y[\bar{1}12]$ direction, the effect of the elastic field of the cavity on the dislocation-vacancy interaction becomes negligible. From the same Fig. 6, we also notice that the vacancy-dislocation interaction energy reaches -0.5 eV at the interface with the cavity. Such a value is to be compared to the energy gain when a vacancy interacts with a preformed jog. From Fig. 4, such a gain is comprised between 0.45 and 0.55 eV depending on the initial position of the vacancy, either situated in the bulk or inside the dislocation core. The good matching between both interaction energies, i.e., the dislocation-vacancy one in the presence of the cavity and the jog-vacancy one, shows that it is certainly the process of jog formation that occurs at the interface of the cavity that anchors a dislocation.

We also computed the migration energy barriers of a vacancy as a function of its distance to an isolated straight dislocation, along x and z. We have limited the jumps of the vacancy to the first neighbors of the fcc crystal. Therefore each vacancy site is associated to 12 transitions [see Fig. 7(a)]. We determined the 12 energy barriers at different initial vacancy positions. We used the NEB method and ART-*nouveau* [61] in order to ease the search of saddle states. We described the methodology employed in Appendix B. The migration energy barriers are plotted against the coordinates X for $n_Z = \pm 1$ in Figs. 7(c) and 7(d) and for $n_Z = \pm 2$ in Figs. 7(e) and 7(f). When $|X|$ is large, the 12 transitions are equivalent and they correspond to the value of the vacancy migration energy in the perfect crystal, i.e., $E_m^{pc} = 0.61$ eV (see Table I). The transitions associated to a jump in the same $(1\bar{1}1)$ plane are represented in Fig. 7 by blue squares while the green triangle pointing downwards represent the vacancy jumps to a lower atomic $(1\bar{1}1)$ plane and the red triangles pointing upwards represent the jumps to a higher $(1\bar{1}1)$ plane. The different shades in symbol colors allow us to distinguish the different directions for same types of jump.

When the vacancy is situated close to the dislocation, i.e., for small $|X|$, the vacancy motion is perturbed by the strain field of the dislocation and the migration barriers diverge from E_m^{pc}. Some are much larger than E_m^{pc} as, for instance, the in-plane jumps (3, 6) at the trailing partial dislocation or the jumps (2, 5) at the leading partial dislocation, that correspond to barriers around 0.95 eV in Fig. 7(c). Some other jumps have barriers much lower than E_m^{pc}, as for instance, the in-plane jump (6) at center of the stacking fault ribbon of the dislocation, which corresponds to a barrier of 0.22 eV in Fig. 7(c). In the $(1\bar{1}1)$ plane $n_Z = 1$ [see Fig. 7(c)], i.e., the plane in which the vacancy is the most stable [see Fig. 5(a)], the lower barriers correspond to the in-plane jumps [see legend in Fig. 7(c)]. In the $(1\bar{1}1)$ plane $n_Z = -1$ [see Fig. 7(d)] and $n_Z = -2$ [see Fig. 7(f)], the in-plane jumps have still the lowest barriers. However, the transitions that correspond to the vacancy migration to upper z plane are also favorable (red triangles pointing upwards). Indeed, a vacancy in the plane $n_Z = 1$ is more stable than in the planes $n_Z = -1$ or $n_Z = -2$, such that vacancies situated in those planes are likely to go to the plane $n_Z = 1$. For the $(1\bar{1}1)$ plane $n_Z = -2$ [see Fig. 7(e)], the lowest energy barriers correspond to jumps toward the plane $n_Z = -1$ (green triangles pointing downwards) where the vacancy is more stable. The same computations for migration energy barriers have been repeated up to $|n_Z| = 8$.

In Fig. 8, we have reported the distribution of the energy barriers that we have computed for the vacancy migration inside the dislocation core. Amongst the different barriers we have identified two possible paths along the dislocation line that correspond to pipe diffusion [13], i.e., to a vacancy migration in y direction inside the dislocation fault ribbon. At low temperatures the vacancy is likely to follow these paths that correspond to the lowest energy barriers. The first path

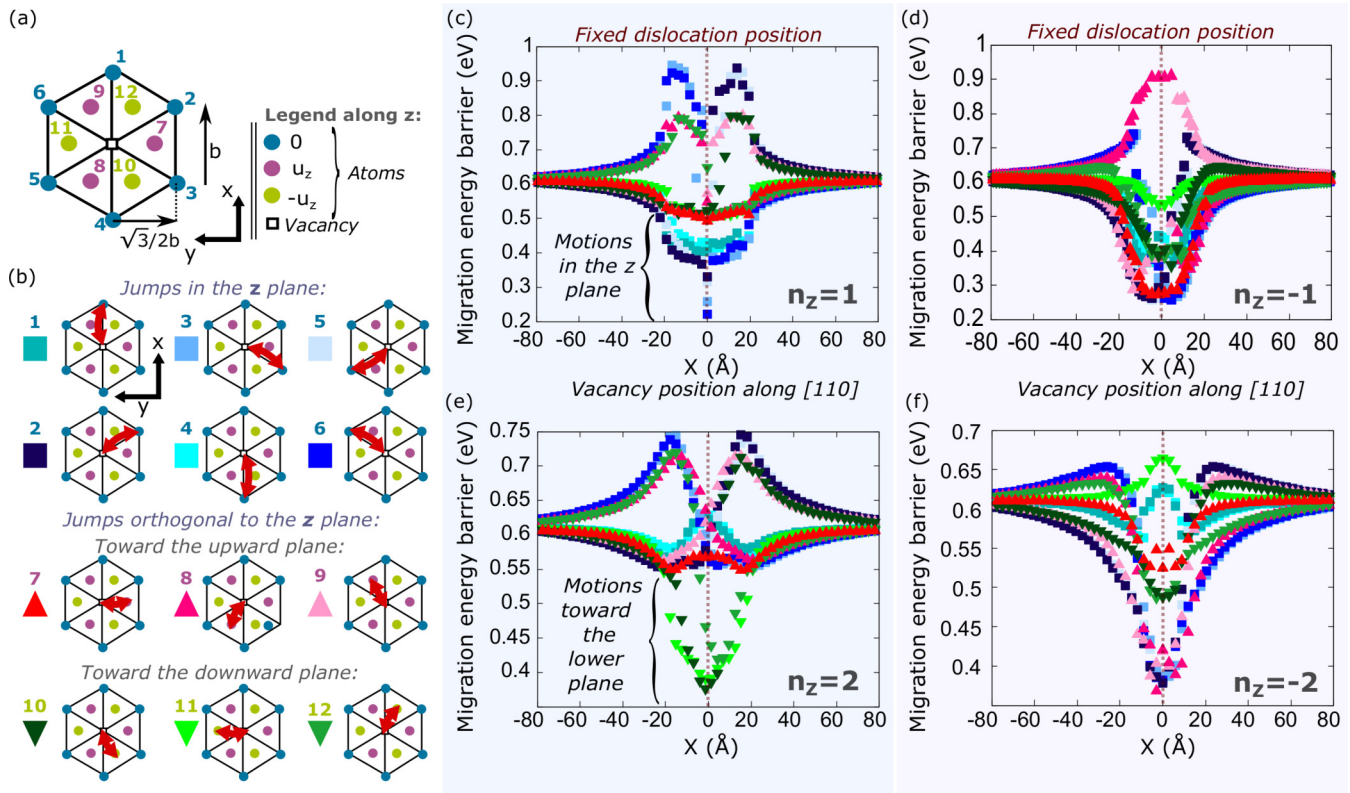

FIG. 7. (a) Schematic representation of the 12 first neighbor atoms (colored circles) of a vacancy (empty square), in the orientation $x[110]$, $y[1\bar{1}2]$, $z[1\bar{1}1]$ for a fcc lattice. The transition denoted by i corresponds to the vacancy migration toward its i^{th} neighbor. The six first neighbors (blue) are in the same $(1\bar{1}1)$ plane while the next three (purple) are situated in the plane above, at a coordinate $u_z = a_0/\sqrt{3}$ and the last three neighbors (green) are situated in the plane below at a coordinate $-u_z$. (b) Schematic representation for the vacancy jumps for the 12 possible migration paths. The numbers correspond to the label of the first neighbor atom defined in (a). (c)–(f) Migration barriers computed through the NEB method, for the 12 transitions shown in (b), against the distance between the dislocation and the vacancy in the $x[110]$ direction and for different distances in $z[1\bar{1}1]$: (c) $n_Z = 1$, (d) n_Z=−1, (e) $n_Z = 2$, (f) n_Z=−2. The blue shaded square symbols are associated to the jump of the vacancy in the same $(1\bar{1}1)$ plane, the green shaded down triangles are associated to the vacancy jumps to lower crystal plane while the red up triangles are associated to the vacancy jumps to the higher crystal plane.

corresponds to successive jumps (2) and (3), allowing the vacancy to migrate in the y direction. At the center of the stacking fault ribbon, in the $(1\bar{1}1)$ plane n_Z= 1 [Fig. 7(c)] these two jumps have energy barriers of 0.3 and 0.25 eV, respectively. The second path we have identified is opposite to the first one as it corresponds to a series of jumps (5) and (6). At the center of the stacking fault ribbon, in the $(1\bar{1}1)$ plane $n_Z = 1$ [Fig. 7(c)] these two jumps have energy barriers of 0.28 and 0.22 eV, respectively. The two different paths have been schematically represented in the inset of Fig. 8. In their experiments, Ogi *et al.* [15] have measured the migration barriers for vacancy diffusion around dislocations through the ultrasonic waves attenuation. They found an energy barrier of 0.28 eV, which is in a rather good agreement with the energy barriers that we have computed for the pipe diffusion. We have reported as vertical straight lines in Fig. 8, the maximum energy barriers associated to the two different paths as well as the measurement from Ogi *et al.*, for comparison.

D. Thermally activated dislocation glide

For a sufficiently large applied shear stress, the dislocation may pass the vacancy cluster within a time much shorter than the typical time for vacancy diffusion processes. The study of such a crossing mechanism is now standard through molecular dynamics [58,62,63] or molecular statics simulations [64,65]. The energy barrier that characterizes the interaction between the dislocation and the vacancy cluster is given by the enthalpy of the system:

$$H(\mathcal{R}) = \Delta U(\mathcal{R}) - \int (\tau_{xz} bL) dx_{\text{dislo}}, \qquad (2)$$

where $\mathcal{R} = (x_{\text{dislo}} - x_{\text{cluster}})$ with x_{dislo} and x_{cluster} as the coordinates of the dislocation and the cluster in the [110] direction, respectively. The integral term in Eq. (2) represents the work of external shear stress τ_{xz}, and $\Delta U(\mathcal{R}) = U(\mathcal{R}) - U(\infty)$ corresponds to the interaction energy, i.e., the difference between the internal potential energy of the simulation cell, $U(\mathcal{R})$, when the distance between the dislocation and the cluster is $\mathcal{R}$ and $U(\infty)$, which is the same but when $\mathcal{R}$ is very large.

To compute $H(\mathcal{R})$ we used the same simulation cell as in Sec. II C [see Fig. 2(a)]. We applied a shear stress $\tau_{xz} = 70$ MPa, sufficient to allow the dislocation to pass the cluster and we integrated the Langevin dynamics as described previously in the text. During the simulations, we periodically

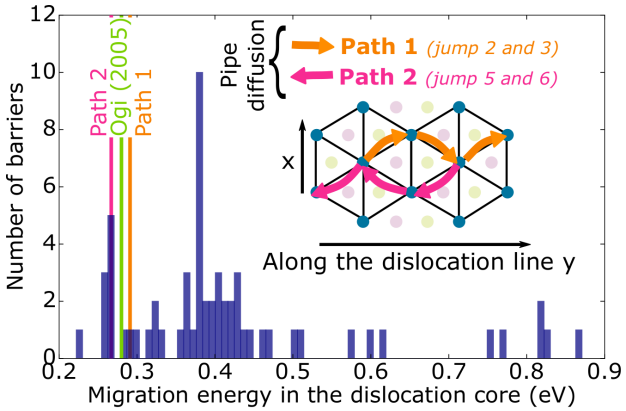

FIG. 8. Distribution of the migration energy barriers in the core of the dislocation defined by $|n_Z| = 1$ and $-8u_x < X < 7u_x$, that corresponds roughly to the positions of the Shockley partials. We have marked the migration energy barrier corresponding to favorable paths (see path 1 and path 2 in the figure legend). Such paths allows pipe diffusion. Our simulation results are compared with the experimental measurements from Ogi *et al.* [15] (green line).

saved the system configuration in order to construct an initial path for the NEB method, which we applied as described in Ref. [38]. We have computed ΔU at various stress levels and we checked that its dependence against the applied shear stress can be neglected. In Fig. 9(a) we have reported the enthalpy variation against the dislocation-vacancy cluster distance, $\mathcal{R}$, in the case of a cluster with a radius of 6.5 Å and a dislocation with a length $L = 119\ b$. Denoting by $\mathcal{R}_M$ and $\mathcal{R}_m$, the distances $\mathcal{R} = (x_{\text{dislo}} - x_{\text{cluster}})$ that corresponds to the maximum $\Delta U(\mathcal{R}_M)$, and to the minimum $\Delta U(\mathcal{R}_m)$ of the internal energy, the activation enthalpy to cross the barrier can be written as

$$\Delta H_{\text{act}} = \Delta U(\mathcal{R}_M) - \Delta U(\mathcal{R}_m) - \tau_{xz} bL(\mathcal{R}_M - R_m). \quad (3)$$

In the absence of applied stress, we identified in Fig. 9(a) that $\mathcal{R}_M$ is situated at 30 Å while $\mathcal{R}_m$ is close to 0. We have repeated the same computations for different cluster sizes and various applied stresses. The activation enthalpy decreases with the applied stress and it increases with cluster size as seen from Fig. 9(b).

The critical shear stress at which ΔH_{act} is zero, denoted by τ_c can be estimated through the theory of Bacon, Kocks and Scattergood (BKS) [66,67] who derived the analytical expression:

$$\tau_c = \frac{\mu_0 b}{2\pi L}\left[\ln\left(\frac{2rL}{(2r+L)b}\right) + B\right], \quad (4)$$

where L is the dislocation length, r is the vacancy cluster radius, and μ_0 is the shear modulus, equal to 25.4 GPa for Al [68]. The parameter B = 0.01 was adjusted to fit the simulation results, which allows us to predict satisfactorily τ_c as shown elsewhere [38]. From Eq. (4), we can derive the maximum pinning force of the vacancy cluster f_p which must satisfy the force balance $f_p = \tau_c bL$. In the standard case of $r << L$, we obtained

$$f_p = \frac{\mu_0 b^2}{2\pi}\left[\ln\left(\frac{2r}{b}\right) + B\right]. \quad (5)$$

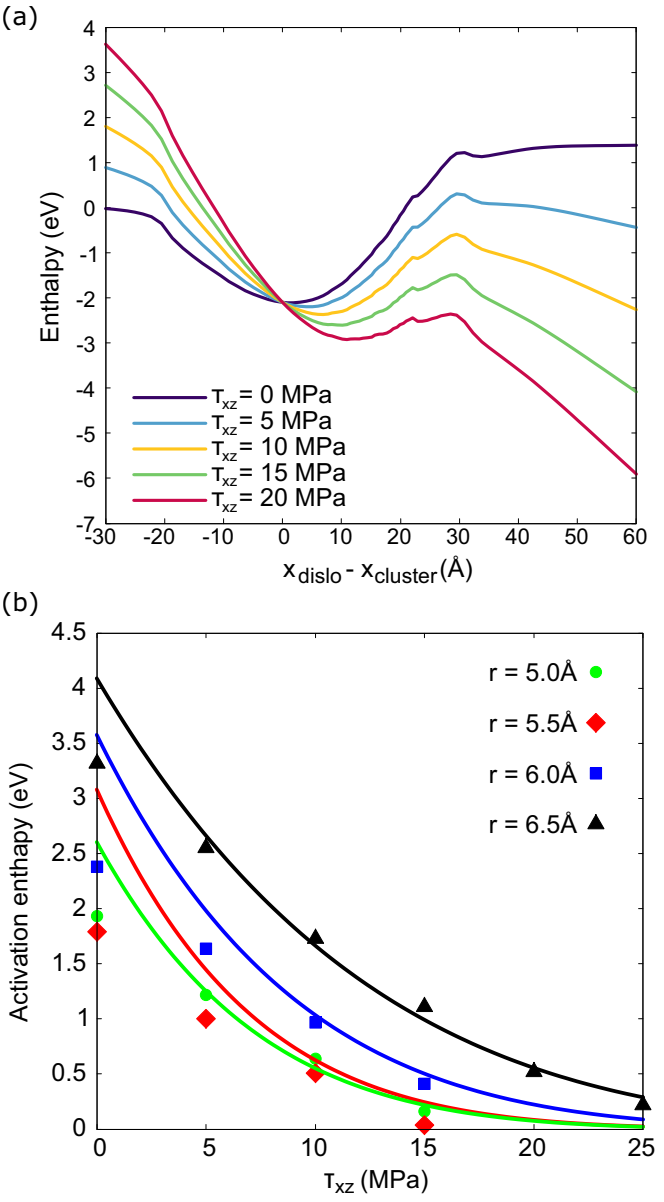

FIG. 9. (a) Enthaply versus dislocation-cluster distance, computed from Eq. (2) for a vacancy cluster of radius $r = 6.5$ Å and a dislocation with $L = 119$ b. (b) Activation enthalpy Eq. (3) computed from simulations (symbols) for several vacancy cluster radius r and computed from the theory Eq. (6) (lines).

In order to model the evolution of the activation enthalpy with the cluster radius, r, and the applied stress, τ_{xz}, we used a phenomenological model of the form

$$\Delta H_{\text{act}} = W_{\text{act}}\left(1 - \frac{\tau_{xz}}{\tau_c}\right)^{p(r)}, \quad (6)$$

where $W_{\text{act}} = 2rf_p$ corresponds to the work of a force f_p (see Eq. (5)) applied over a distance equivalent to the cluster diameter $2r$ and $p(r)$ is a parameter that follows the empirical form:

$$p(r) = 1 + \left(\frac{\kappa_1 b}{r}\right)^3 \exp\left(-\kappa_2\left(\frac{b}{r}\right)^{\kappa_3}\right), \quad (7)$$

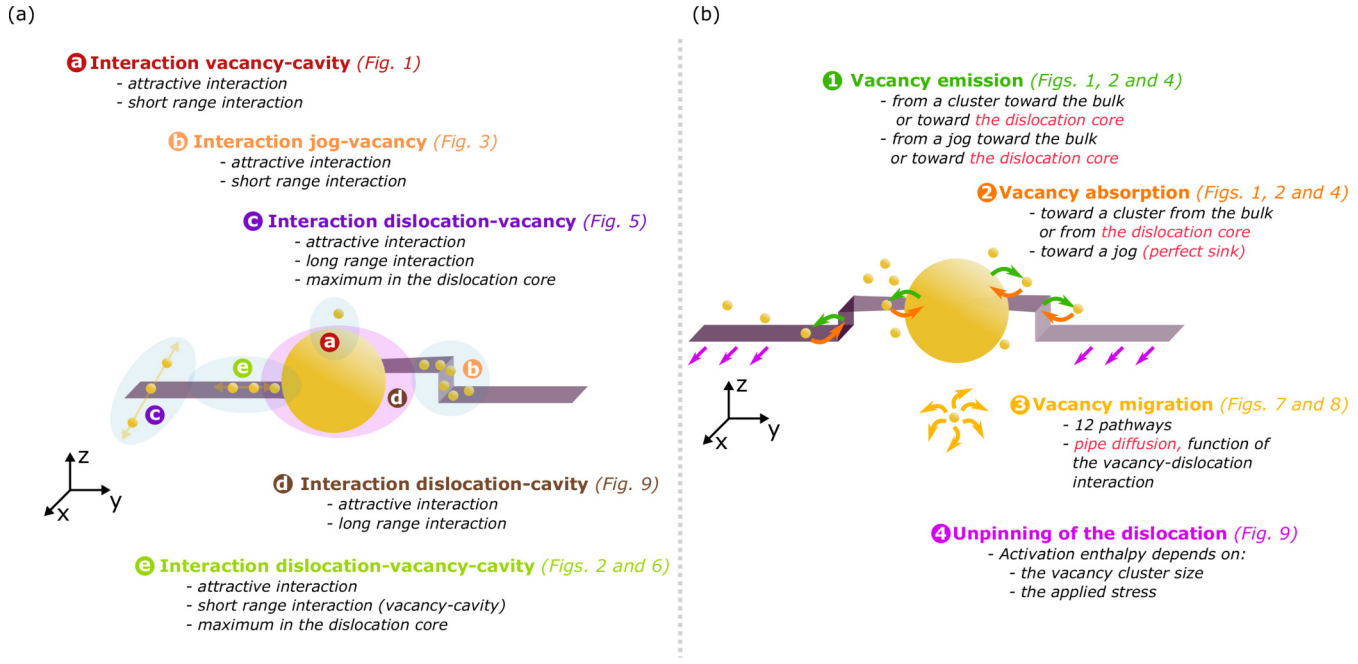

FIG. 10. (a) Summary of all the possible interactions deduced from our atomic scale simulations. Each interaction in the schematic is quoted by a colored encircled letter. (b) Schematic representation of the four types of kinetic events that we considered in the KMC-ELM. The colors of arrows are associated to the event type. The more favorable events are emphasized with a red font.

with $\kappa_1 = 3.69$, $\kappa_2 = 538$, and $\kappa_3 = 14$, three parameters with no physical signification, adjusted to reproduce the simulation data. Note that $p(r)$ decreases as the vacancy cluster size increases and tends to 1 for large clusters. Thence for large clusters, the physical meaning of Eq. (6) becomes clear. When the applied stress $\tau_{xz} = 0$, then $\Delta H_{\text{act}} = W_{\text{act}}$ it is given the minimal work required to pass a pinning force f_p, which would be exerted over a distance of $2r$. When $\tau_{xz} > 0$ the activation enthalpy decreases linearly in τ_{xz} with a typical activation volume given by W_{act}/τ_c. As seen from Fig. 9(b), the model allows us to reproduce rather well the simulation results. We have summarized all the interactions and the possible events that we have deduced from our atomic scale simulations in Fig. 10. The totality of those events were incorporated in the KMC-ELM simulations presented in Sec. III. In particular the variation of the migration barrier for the vacancy according to its position in the simulation cell, i.e., its distance to the dislocation and to the cavity were taken into account carefully.

E. Analysis of molecular static simulations

Here we have to analyze our MS results in more details since according to Fig. 6 the situation of a vacancy situated at the interface between a dislocation and a cavity is more stable than other vacancy positions in the simulation cell; meanwhile according to Fig. 2(b), the process of leaving such an interface is favored since the configuration $\mathcal{P}_4$ is -0.24 eV lower than $\mathcal{P}_1$. The two results seem to contradict. In the same vein a similar contradiction could be seen in the comparison between Fig. 2 and both Figs. 1 and 5. From Fig. 1, the interaction energy between a vacancy and a cavity is -0.2 eV while from Fig. 5 the interaction energy between a vacancy and a dislocation is at best -0.18 eV. The subtraction between these two energies would lead to a difference of 0.02 eV, which could be interpreted as that the energy landscape for the vacancy to leave a cavity and migrate inside the dislocation core should be uphill. From Fig. 2(b) we notice that it is not the case.

We have now all information that permits us to clarify such an apparent contradiction between a vacancy energy landscape that would be more stable at the interface of the cavity, and the instability of a cavity in contact with a dislocation. Such a dissolution is confirmed through KMC-ELM simulations in the next section. The net driving force for such a process is analyzed as follows.

We defined the energy of our simulation cell containing a single vacancy and a cavity made of n vacancies through $E[\text{Cav}_n\ \infty\ V]$ when the vacancy and the cavity are situated far away from each other. In contrast, when the vacancy is situated at the periphery of the cavity such an energy is then given by $E[\text{Cav}_n\ 0\ V]$. The symbols Cav_n and V represent the cavity and the vacancy, respectively, while the symbols ∞ and 0 define their distances. According to Fig. 1 the interaction energy between the cavity and the vacancy is

$$E[\text{Cav}_n \quad \infty \quad V] - E[\text{Cav}_n \quad 0 \quad V] = -0.2\ \text{eV}. \tag{8}$$

In a similar manner, we defined the interaction energy between a vacancy (V), a cavity (Cav_n) and a dislocation (D). Since we have now three bodies we denoted the simulation cell energy as a table :

$$E\begin{bmatrix} & D & \\ \infty & & \infty \\ \text{Cav}_n & \infty & V \end{bmatrix}, \tag{9}$$

when the vacancy, the dislocation, and the cavity are situated far away from each other. The symbols between each pair of objects (D, Cav_n, V) represent the distance between them. When the vacancy is at the periphery of the cavity and the dislocation is far away the simulation cell energy is then represented by

$$E\begin{bmatrix} & D & \\ \infty & & \infty \\ \mathrm{Cav}_n & 0 & V \end{bmatrix}. \tag{10}$$

Since in the two previous cases the dislocation is far from the cavity and from the vacancy the dislocation does not modify the interaction between the cavity and the vacancy and we thus deduce from Eq. (8) that

$$E\begin{bmatrix} & D & \\ \infty & & \infty \\ \mathrm{Cav}_n & \infty & V \end{bmatrix} - E\begin{bmatrix} & D & \\ \infty & & \infty \\ \mathrm{Cav}_n & 0 & V \end{bmatrix} = -0.2\ \mathrm{eV}. \tag{11}$$

The energy of the simulation cell containing a dislocation and a vacancy situated far away from each other was also defined by

$$E\begin{bmatrix} D \\ \infty \\ V \end{bmatrix}, \tag{12}$$

whereas we defined through

$$E\begin{bmatrix} D \\ 0 \\ V \end{bmatrix} \tag{13}$$

the energy of the simulation cell when the vacancy is situated at the more stable position inside the fault ribbon of the dislocation, in the crystal plane just above the glide plane. According to Fig. 5(a) we have

$$E\begin{bmatrix} D \\ \infty \\ V \end{bmatrix} - E\begin{bmatrix} D \\ 0 \\ V \end{bmatrix} = -0.18\ \mathrm{eV}. \tag{14}$$

We also defined through

$$E\begin{bmatrix} & D & \\ \infty & & 0 \\ \mathrm{Cav}_n & \infty & V \end{bmatrix} \tag{15}$$

the simulation cell energy for a cavity situated far away from a vacancy and from the dislocation, while the vacancy is situated at the more stable position inside the dislocation core. Then we can write

$$E\begin{bmatrix} & D & \\ \infty & & \infty \\ \mathrm{Cav}_n & \infty & V \end{bmatrix} - E\begin{bmatrix} & D & \\ \infty & & 0 \\ \mathrm{Cav}_n & \infty & V \end{bmatrix} = -0.18\ \mathrm{eV}, \tag{16}$$

since the cavity is far from the dislocation and from the vacancy and thence the cavity does not interact with the dislocation and the vacancy. The difference between Eq. (16) and Eq. (11) gives

$$\begin{aligned} S_a = {} & E\begin{bmatrix} & D & \\ \infty & & \infty \\ \mathrm{Cav}_n & \infty & V \end{bmatrix} - E\begin{bmatrix} & D & \\ \infty & & 0 \\ \mathrm{Cav}_n & \infty & V \end{bmatrix} \\ & - E\begin{bmatrix} & D & \\ \infty & & \infty \\ \mathrm{Cav}_n & \infty & V \end{bmatrix} + E\begin{bmatrix} & D & \\ \infty & & \infty \\ \mathrm{Cav}_n & 0 & V \end{bmatrix}, \end{aligned} \tag{17}$$

which leads to the following result:

$$\begin{aligned} S_a = {} & E\begin{bmatrix} & D & \\ \infty & & \infty \\ \mathrm{Cav}_n & 0 & V \end{bmatrix} - E\begin{bmatrix} & D & \\ \infty & & 0 \\ \mathrm{Cav}_n & \infty & V \end{bmatrix} \\ = {} & -0.02\ \mathrm{eV}. \end{aligned} \tag{18}$$

Such a quantity, denoted by S_a corresponds to the energy required to remove a vacancy from an isolated cavity and to place it inside a dislocation fault ribbon situated far away from the cavity. Such a process is not favorable since $S_a < 0$ and therefore we can conclude that the vacancy segregation on cavities is more propitious than the segregation on dislocation, even though we have to admit that the difference is rather small. Of course, such a conclusion depends dramatically on the EAM interatomic potential and it requires to be confirmed by different MS simulations with different interatomic potentials or different simulation methods.

To estimate the binding energy of a vacancy with the dislocation-cavity interface in comparison to the case where the vacancy is situated inside the dislocation core far from such an interface, the quantity S_a is not appropriate since the dislocation and the cavity are in contact and their interaction also varies according to the presence of the vacancy. To compute the binding energy of a vacancy with the dislocation-cavity interface in comparison to the case where the vacancy is situated inside the dislocation core far from such an interface, we introduced

$$S_b = E\begin{bmatrix} & D & \\ 0 & & 0 \\ \mathrm{Cav}_n & 0 & V \end{bmatrix} - E\begin{bmatrix} & D & \\ 0 & & 0 \\ \mathrm{Cav}_n & \infty & V \end{bmatrix}, \tag{19}$$

where the first term corresponds to the simulation cell energy when the vacancy is situated at the interface between the dislocation and the cavity (configuration $\mathcal{P}_1$ in Fig. 2) and the second term corresponds to the energy of the simulation cell where the dislocation is anchored by the cavity and the vacancy is situated inside the dislocation core far away from the cavity (at the more stable position in the dislocation fault ribbon). We compute the difference $S_b - S_a$ between Eq. (19) and Eq. (18), which gives

$$\begin{aligned} S_a - S_b = {} & E\begin{bmatrix} & D & \\ 0 & & 0 \\ \mathrm{Cav}_n & \infty & V \end{bmatrix} - E\begin{bmatrix} & D & \\ \infty & & 0 \\ \mathrm{Cav}_n & \infty & V \end{bmatrix} \\ & + E\begin{bmatrix} & D & \\ \infty & & \infty \\ \mathrm{Cav}_n & 0 & V \end{bmatrix} - E\begin{bmatrix} & D & \\ 0 & & 0 \\ \mathrm{Cav}_n & 0 & V \end{bmatrix}. \end{aligned} \tag{20}$$

On the first line we recognize the interaction energy between a dislocation and a cavity of size n, since the vacancy is situated

far away from the cavity along the dislocation core. It plays no role in the interaction between the cavity and the dislocation. This first line is therefore equal to

$$E\begin{bmatrix} D \\ 0 \\ \mathrm{Cav}_n \end{bmatrix} - E\begin{bmatrix} D \\ \infty \\ \mathrm{Cav}_n \end{bmatrix}, \tag{21}$$

which corresponds to the binding energy between a dislocation and a cavity containing n vacancies. Such a quantity is negative since the interaction between a dislocation and a cavity is attractive (see Fig. 9). On the second line of Eq. (20) we recognize the interaction energy between a dislocation and a cavity of size $n+1$:

$$E\begin{bmatrix} D \\ 0 \\ \mathrm{Cav}_{n+1} \end{bmatrix} - E\begin{bmatrix} D \\ \infty \\ \mathrm{Cav}_{n+1} \end{bmatrix}, \tag{22}$$

since when the distance between a vacancy and the cavity is zero we can consider that both form a single cavity.

We thus conclude that $S_a - S_b$ is simply the variation of dislocation-cavity interaction energy according to the cavity size:

$$S_a - S_b = E\begin{bmatrix} D \\ 0 \\ \mathrm{Cav}_n \end{bmatrix} - E\begin{bmatrix} D \\ \infty \\ \mathrm{Cav}_n \end{bmatrix} - \left(E\begin{bmatrix} D \\ 0 \\ \mathrm{Cav}_{n+1} \end{bmatrix} - E\begin{bmatrix} D \\ \infty \\ \mathrm{Cav}_{n+1} \end{bmatrix} \right). \tag{23}$$

The interaction energy between a cavity and a dislocation decreases in amplitude when the size of the cavity decreases since the interaction energy of a dislocation with a unique vacancy is obviously smaller than the interaction energy with a cluster made of many vacancies. For small clusters the geometry is to be taken into account but our analysis is intentionally simplified to reproduce the main trend. We deduce that

$$E\begin{bmatrix} D \\ 0 \\ \mathrm{Cav}_n \end{bmatrix} - E\begin{bmatrix} D \\ \infty \\ \mathrm{Cav}_n \end{bmatrix} > E\begin{bmatrix} D \\ 0 \\ \mathrm{Cav}_{n+1} \end{bmatrix} - E\begin{bmatrix} D \\ \infty \\ \mathrm{Cav}_{n+1} \end{bmatrix}, \tag{24}$$

which allows us to conclude that in general $S_a - S_b > 0$. In order to evaluate $S_a - S_b$ we used the MS data obtained in Fig. 9(a) with no applied stress, i.e., $\tau_{xz} = 0$. The energy difference between the configuration at distance $(x_{\mathrm{dislo}} - x_{\mathrm{cluster}}) = -30$ Å and $(x_{\mathrm{dislo}} - x_{\mathrm{cluster}}) = 0$ Å provides us a good estimation of the interaction energy between the dislocation and the cluster. In Fig. 9 the interaction energy is -2.55 eV for a cluster size equivalent to $r = 6.5$ Å, that corresponds to a number of $n = 71$ vacancies. We repeated the same type of computation for a cavity of radius $r = 5.5$ Å, which is equivalent to $n = 43$ vacancies and we obtained an interaction energy of -0.91 eV. From a linear regression we deduced that the variation between the interaction energy for n and n+1 is therefore around 0.06 eV, which means $S_a - S_b \approx 0.06$ eV and thus $S_b \approx -0.08$ eV, which means that a vacancy is more stable at the contact of a cavity than situated alone in the dislocation core.

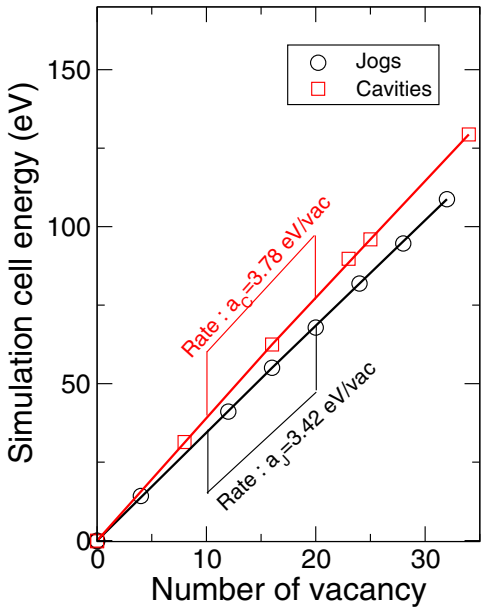

FIG. 11. Variation of the simulation cell potential energy according to the number of vacancy required to build either a pair of jogs or a cavity situated right on the edge type dislocation core. The distance between the jogs and varies according to the number of vacancy as well as the cavity radius.

However, another contribution to the vacancy energy landscape must be accounted for since when the vacancies accumulate along the edge dislocation line they may form some jogs (see Fig. 3). In order to simplify and to provide a clear line of reasoning, we avoid discussing the primary stage of jogs formation from a cavity. In such a complex process we have to be confident in simulations. Nevertheless we can yet figure out what the vacancy energy landscape is in presence of a cavity and well formed jogs. In Fig. 11 we have reported the energy variation of the simulation cell according to the number of vacancy required to build a pair of jog on the edge dislocation. The distance between the jogs is adapted to the number of vacancy needed. In the same Fig. 11, we compared our results to the energy variation of the simulation cell containing a cavity in interaction with an edge type dislocation. We reported the results according to the number of vacancy involved in the cavity or in the pair of jog. We denoted that number by n and we remarked that the pair of jog is more stable than the cavity for every n. The energy variations are linear in n for both cavities and jogs and we denoted by a_C and a_J the energy rate variation for cavities and jogs, respectively. We deduced that in a simulation cell containing a dislocation that bears a pair of jog corresponding to n_J vacancies, and where the dislocation is anchored by a cavity made of n_c, the energy of the system can be approximated by $E = a_C n_C + a_J n_J$. When a vacancy moves from the cavity to a jog the simulation cell energy becomes $E = a_C(n_C - 1) + a_J(n_J + 1)$. The energy variation between the final state and the initial state is simply $S_c = a_J - a_C = -0.36$ eV. We assume that this energy gain due to the expansion of jog S_c at the expense of cavity can be superimposed to the vacancy segregation on a simple dislocation $-S_b$. In both cases the vacancy is removed from a cavity and put inside the dislocation core. It means that a

vacancy that would leave a cavity to travel inside the dislocation core would cost $-S_b = 0.08$ eV to the system but it would yield a gain of $S_c = -0.36$ eV through its participation to a jog. The energy balance sheet is thus -0.28 eV in favor of the dissolution of cavities to form jogs. Such a value is in quite good agreement with the gain of -0.24 eV reported in Fig. 2, obtained when a vacancy makes one single jump away from the cavity. Such a small discrepancy could be ascribed to the strong approximations made along the present analysis as the MS computations are far more accurate. Nevertheless the essential contributions are captured by our general reasoning and our discussion allows us to conclude that the driving force for the dissolution of cavities in contact with dislocations is essentially due to the formation and the expansion of jogs. In what follows we shall use the barrier shown in Fig. 2 as representative of the vacancy landscape to leave a cavity and we shall assume that once such a barrier has been crossed the vacancy energy landscape is described by the energy barriers in the isolated dislocation core (as shown in Fig. 7) up to meet a jog where the energy barriers are then given by Fig. 4(b). We admit that a more refined knowledge of the vacancy landscape around the cavity-dislocation interface would be needed to complete our work but the very large number of data already accumulated compels us to postpone such a tedious task. The general analysis presented above permits us to confirm that our approximation should be reasonable since the different escape paths of vacancies should remain rather close from the one shown in Fig. 2.

III. KINETIC MONTE CARLO ELASTIC LINE MODEL

In order to perform simulations where the dislocation may glide and where the vacancy diffusion processes are accounted for, we developed a method based on the combination of two models: KMC model [26] and the ELM [27,69–71]. In order to describe the distribution of clusters and vacancies we identified the atomic sites of a standard fcc lattice with same orientation as the atomic scale simulations presented in the previous section. For practical computational purpose, we have mapped the fcc crystal on an orthorombic lattice. Each node of the latter is separated from its nearest neighbor by a distance $u_x = b/2$, $u_y = b\sqrt{3}/2$ and $u_z = a_0/\sqrt{3}$, in x, y, and z directions, respectively [see Fig. 12(a)]. Among the orthorombic lattice sites we selected only those that correspond to the fcc lattice in order to define the possible positions of the vacancies and their clusters. The dislocation is represented by an elastic line that is discretized with a series of segment constrained to move along the rows of the orthorombic lattice in the plane at the coordinate 0. Each segment of the line is identified by the number of the row along which it moves. The position of the segment number l along the x axis is given by the function $x(l)$. A difference in the positions of segments l and $(l+1)$ yields a variation of potential energy associated to the line tension [72]. In the harmonic approximation, we expressed such a contribution [73] as $\Delta E_l = \Gamma(x_{l+1} - x_l)^2/2u_y$. In order to account for the dissociation of the dislocation, along each row of the lattice we identified the atomic sites situated at a distance inferior to the dissociation distance d_{ed} [see Table I and Fig. 12(b)]. The n_d selected sites correspond to energy and migration barriers for the vacancies that were

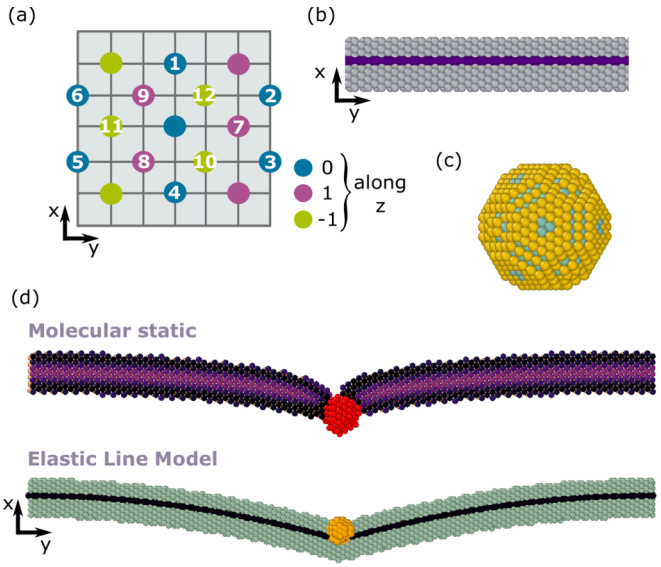

FIG. 12. (a) Mapping of the fcc crystal on an orthorombic lattice. The orientation is the same as for MS simulations in Fig. 3. The orthorombic lattice unit vectors are defined in the text. The possible atomic sites of the fcc crystal are represented by circles. The 12 first neighbors of the crystal site situated at center of the figure are labeled by numbers. (b) Segment of dislocation simulated in the ELM. The elastic line is colored in purple while the atoms of the lattice associated to the dislocation ribbon are colored in grey. They are selected according to their distance to the line, inferior to d_{ed} (see Table I). (c) A vacancy cluster reproduced in orthorombic lattice used to perform kinetic Monte Carlo (KMC) simulations. The vacancies inside the cluster are colored in green while those at the surface are colored in yellow. (d) Comparison between a dislocation line of length $L = 29$ nm anchored by a vacancy cluster of radius $r = 6$ Å, simulated through MS simulations described in previous sections and through bridging KMC and ELM. The applied shear stress is $\tau_{xz} = 49$ MPa. In the KMC-ELM model the neighbors of the void (colored in red in the MS) are not represented, which explains the seeming different sizes of obstacles.

determined through MS. The vacancies are now identified individually by their positions on the orthorombic lattice. The vacancy clusters are made of an assembly of vacancies [see Fig. 12(c)]. The radius of the cluster is related to the pinning force f_p through Eq. (5). Since only the vacancies situated at the surface of the clusters may move, they are identified along the simulation and selected for possible motion in KMC.

The position of the dislocation segment along row number l is given by the coordinate x_l along the glide direction $x[110]$ and z_l along the climb direction $z[1\bar{1}1]$. In the $(1\bar{1}2)$ lattice plane containing the row number l we identified the clusters by a label n_l and the coordinates of the clusters centers $x_{n,l}$ and $z_{n,l}$. The distance $\mathcal{R}_{n,l}$ between the elastic line and the cluster n_l is then given by

$$\mathcal{R}_{n,l} = \sqrt{(x_l - x_{n,l})^2 + (z_l - z_{n,l})^2}. \tag{25}$$

The interaction between a dislocation segment and the vacancy cluster was modeled with an attractive potential of the form $W(\mathcal{R}_{n,l}) = -A(\mathcal{R}_{n,l}^2 - w^2)^4/w^8$ where $A = 343\sqrt{7}w f_p(r)/1728$ is the amplitude of the potential and w is

the cutoff distance above which the interaction is disregarded. We choose $w = \varsigma r$ with $\varsigma = 1.1$. The main purpose of such a simple potential is to reproduce the attractive pinning force of the cluster according to its size and the range of the interaction. The variation of the pinning force, $f_p(r)$ with the cluster size r is described by the BKS theory [see Eq. (5)].

The total force on a line element l writes as follows:

$$F_l = \tau_{xz} b u_y + \Gamma(x_{l+1} + x_{l-1} - 2x_l)/u_y - \sum_{n_l} W'(\mathcal{R}_{n,l}), \tag{26}$$

where the first term corresponds to the Peach-Koehler force [74] on segment l, the second term represents the line tension contribution and the third term represents the interaction with the series of clusters in the plane perpendicular to the segment. The line tension was adjusted to $\Gamma = 9$ eV/nm in order to reproduce the curvature of the dislocation line observed in our MS computations[27] (see Fig. 12(d)). The line tension determined throughout standard elastic theory [72] is $\Gamma_{el} = 2.7$ eV/nm [38]. If the applied stress is lower than the critical shear stress, the force F_l in Eq. (26) tends to zero after several step of relaxation algorithm, i.e., the simple gradient algorithm. The relaxation was supposed to be reached when the forces are inferior to 10^{-11} eV/nm. Once the force relaxation was achieved, we run the KMC algorithm to simulate the thermally activated processes. The different processes that are accounted for are presented in Fig. 10(b).

The vacancy emission process is represented by green arrows in Fig. 10(b). According to our MS computations the most favorable sources of vacancies are the vacancy clusters. The vacancies may form at the vacancy cluster surfaces and migrate to the crystal or directly at the interface between the dislocation core and the cavity (see Figs. 1 and 2). According to Fig. 7, the most favorable process is the emission of vacancies from the cluster at the interface. Vacancies could also form at the dislocation jogs (see Fig. 4) but such a process is less favorable than the emission from vacancy clusters. The vacancy absorption process is represented by orange arrows in Fig. 10(b). We assumed that when a vacancy escapes from a cavity and moves along the dislocation-cluster interface it contributes to the formation and then the expansion of a jog, eventually. Such an hypothesis is also supported by a former work (see Fig. 4 in Ref. [38]). The interface dislocation-vacancy cluster is therefore a favorable place to initiate the formation of a jog.

When a vacancy escapes from a cavity inside the dislocation core we assumed that a jog is formed on the dislocation unless a jog is already present. We have verified that a higher jog in z direction is not favorable. If a jog is already present then the vacancy contributes to extend the jog by one atomic distance in y direction. It requires, therefore, the diffusion of the vacancy until it reaches the tip of the jog. The most favorable path and the shortest one is along the dislocation core, via the pipe diffusion (see Fig. 8). When a vacancy is situated at one interatomic distance of a stair-rod dislocation, we also assumed that it is instantaneously absorbed by the line since the MS simulations show that such a dislocation segment is a perfect sink (see Fig. 3). The jog associated to the stair-rod dislocation is then shifted by one atomic distance in the y direction. The vacancies can also be absorbed when they are situated in the vicinity of a vacancy cluster. The absorption is not spontaneous since it corresponds to some barriers computed in MS simulations (see Figs. 1 and 2). The vacancy migration process [see yellow arrows in Fig. 10(b)] occurs with 12 possible transitions corresponding to label numbers in Figs. 7(a) and 7(b). The associated energy barriers were extracted from Figs. 7(c) and 7(e). According to MS computations the diffusion is isotropic for large dislocation-vacancy distances but certain directions are favored when the vacancy is situated in the $(1\bar{1}1)$ planes that bound the dislocation glide plane. When the applied shear stress is much smaller than the critical stress threshold, the glide of the dislocation [see purple arrows in Fig. 10(b)] is very unlikely. Such a mechanism becomes possible when the applied stress approaches the critical stress. Along the KMC-ELM simulations, the size of the cluster evolves through emission or absorption of vacancies. Consequently the activation enthalpy barrier for dislocation glide, ΔH_{act}, also evolves as the radius and therefore the pinning strengths of the clusters vary in time [see Eq. (6)]. Because of pipe diffusion the shape of the clusters changes and flattens (see Fig. 18). Then it is difficult to estimate the evolution of the pinning force as a function of a geometric radius, as for a sphere. We hypothesized that the pinning force of a cluster, containing N_v vacancies, is similar to an equivalent spherical cluster of N_v vacancies. This hypothesis should be verified in the future, but it seems reasonable even for clusters with nonspherical forms according to Ref. [65]. The equivalent radius r_{eq} is thus given by

$$r_{\text{eq}} = \left(\frac{3}{4\pi} N_v v_{\text{at}}\right)^{(1/3)}, \tag{27}$$

with v_{at} as the atomic volume. In Al, $v_{\text{at}} = 1.66 \times 10^{-29}$ m^3. The equivalent radius r_{eq} was used to estimate the pinning force through BKS theory Eq. (5). Once all the possible events have been listed, we estimated the probability to realize each event via the frequency $p_{\text{init}\to\text{final}}$, where the subscripts (init) and (final) stand for the initial and final states, respectively. The frequency of each event is determined through the Arrhenius law:

$$P_{\text{init}\to\text{final}} = \nu \exp\left(-\frac{E_{\text{act}}}{k_B T}\right), \tag{28}$$

where $\nu \simeq 10^{13}\text{s}^{-1}$ corresponds roughly to the Debye frequency of solid and E_{act} represents the activation energy barrier associated to the concerned event, i.e., listed in Fig. 10(b). In the case of the thermal activation of dislocation crossing, E_{act} takes the value of the activation enthalpy computed in Sec. II.

Following the KMC algorithm [26], the event at k^{th} rank in our list, containing $\mathcal{Q}$ possible events, is selected provided that the computationally generated random number $r_1 \in]0, 1]$ falls in the interval

$$\mathcal{S}_{k-1} < r_1 \mathcal{S}_{\mathcal{Q}} < \mathcal{S}_k, \tag{29}$$

where $\mathcal{S}_k$, $\mathcal{S}_{k-1}$, and $\mathcal{S}_{\mathcal{Q}}$ are the sums of event frequencies given by

$$\mathcal{S}_k = \sum_{u=1}^{k} P_{\text{init}\to\text{final}}. \tag{30}$$

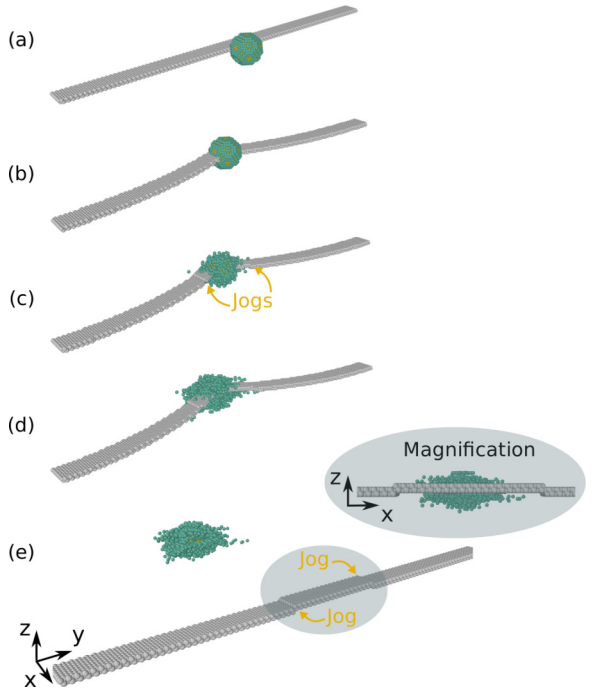

FIG. 13. (a)–(e) Snapshots of configurations in KMC-ELM simulations for a vacancy cluster of radius r=19 Å, at $T=$ 400 K, $\tau_{xz} = 50$ MPa and for a line length $L = 160\ b$. (a) The dislocation is straight, i.e., not in interaction with the cluster. (b) Under the effect of applied stress the dislocation glides and it encounters the cluster. (c),(d) Configurations obtained during the kinetic process of vacancy diffusion. Two opposite jogs are formed. (e) The glide of the dislocation with jogs is thermally activated and the dislocation passes the vacancy cluster, which became ovoid because of pipe diffusion.

Once selected, the corresponding transition is realized and the elastic line forces are relaxed every 100 events such that the elastic line could find the next nearest anchored configuration. The time t is incremented by $\delta t = \frac{\ln r_2}{\mathcal{S}_\mathcal{Q}}$, where $r_2 \in]0, 1]$ is a second random real number [26]. During the simulation, the size of the vacancy cluster evolves and we therefore recomputed the new pinning forces of the clusters. In KMC-ELM simulations, the vacancy-vacancy interactions were ignored, which constitutes an approximation to be studied carefully later on.

Our simulation cell size is $160b$ in three directions of space. The simulations have shown that a local climb process occurs in the vicinity of the cluster, with the formation of two jogs [see Figs. 13(c)–13(e)]. Such a climb is driven by the complex dislocation-vacancy interaction which leads to the jog formation and expansion. The kinetic path for this process depends therefore on the local environment of the vacancy (see Fig. 10). As the cluster size reduces because of vacancy absorption by jogs, the pinning force of the cluster decreases [see the color dots in Figs. 14(a)–14(c)].

In order to obtain a satisfactory sampling, we have repeated the same simulations 50 times with different series of random numbers which explains the dispersion of the data shown in Figs. 14(a)–14(c).

In order to rationalize the pinning strength decrease computed through KMC-ELM. We considered that the vacancies

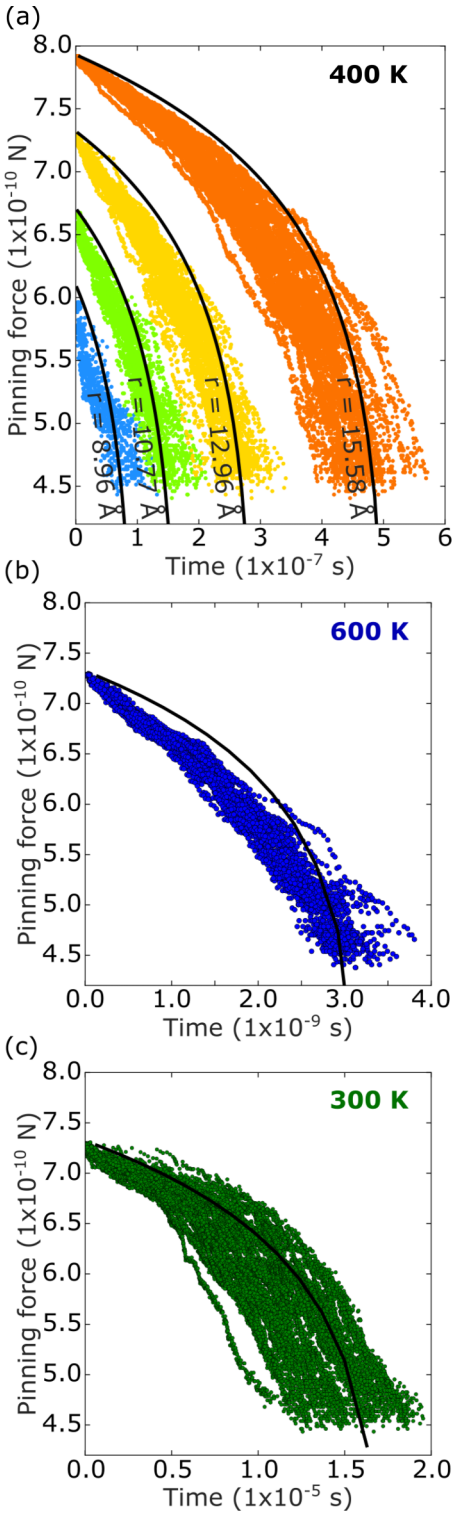

FIG. 14. (a) Cluster pinning force decrease versus time for several cluster radius r at $T = 400$ K and 50 different series of random numbers in KMC-ELM. (b) Same as in (a) but for $r = 12.96$ Å at $T = 600$ K. (c) Same as in (b) but for $T = 300$ K. Comparison between KMC-ELM results (color dots) and the empirical fit in Eq. (33) (black line).

are emitted from the cluster into the dislocation core through two contact points that intend to represent the interface dislocation/cluster and that the vacancy cluster reduces in size

with the following frequency:

$$\Omega = 2\nu \exp\left(-\frac{G_{\rm act}}{k_B T}\right), \tag{31}$$

where $G_{\rm act}$ corresponds to an activation barrier which intends to account in a time independent manner the vacancy emission along the process of cluster evaporation. Since Ω is also by definition the derivative of the number of vacancy contained in the cluster against time we identified Ω to $\frac{4\pi r^2}{v_{\rm at}}\frac{dr}{dt}$, which yields

$$r(t) = \sqrt[3]{r_0^3 - \frac{3v_{\rm at}}{4\pi}\Omega t}, \tag{32}$$

and once combined with Eq. (5) gives

$$f_p(t) = \frac{\mu_0 b^2}{6\pi}\left[\ln\left(\frac{8r_0^3}{b} - \frac{6v_{\rm at}}{\pi b^3}\Omega t\right) + 3B\right]. \tag{33}$$

The activation energy, $G_{\rm act}$, is adjusted to fit in a phenomenological manner the KMC-ELM results. We obtained the best agreement [see lines in Figs. 14(a)–14(c)] with $G_{\rm act}$ written as a polynomial regression of temperature $G_{\rm act} = b_0 + b_1 k_B T + b_2 (k_B T)^2$, where $k_B T$ is expressed in eV and the coefficients are $b_0 = 0.38$ eV, $b_1 = -0.1$ and $b_2 = -48$ eV^{-1}. The fact that the coefficients b_1 and b_2 are negative seems to indicate that the energy barrier for the vacancy emission decreases when the temperature increases, while the energy barriers in KMC-ELM simulations do not vary with temperature. It is worth noticing that such a variation cannot be ascribed to the vibrational entropy since KMC-ELM barriers have been fixed according to zero temperature MS computations. The only entropy contribution present in our KMC-ELM model is the configurational one. The effective decrease of the adjusted barrier $G_{\rm act}$ is related to the fact that various events, with different activation energy, occur in the vicinity of the cavity (emission of vacancies toward the bulk and the dislocation core, absorption of vacancy). At low temperatures only the most favorable events occur contrary to high temperatures where all type of events can occur more easily. Then it is natural that the activation energy $G_{\rm act}$ depends on the temperature. We believe that the present approach could certainly be improved in the future to avoid the adjustment of $G_{\rm act}$.

In the simulation of KMC-ELM, the dislocation can pass the vacancy cluster after a while. By repeating such simulations with different random series, we have been able to determine the average waiting time t_D, during which a dislocation is anchored. In Figs. 15(a)–15(c) the error bars of our simulation points correspond to the standard deviation for a sampling of 50 simulations.

In Fig. 15(a) we notice that the waiting time t_D decreases when the applied stress τ_{xz} increases up to the critical stress threshold τ_c. Since τ_c depends on both the cluster size r and the dislocation length L [see Eq. (4)] we analyzed how t_D varies with respect to r [see Fig. 15(a)], L [see Fig. 15(b)], and the temperature T [see Fig. 15(c)]. In order to rationalize our simulation results, we fitted them with an analytic

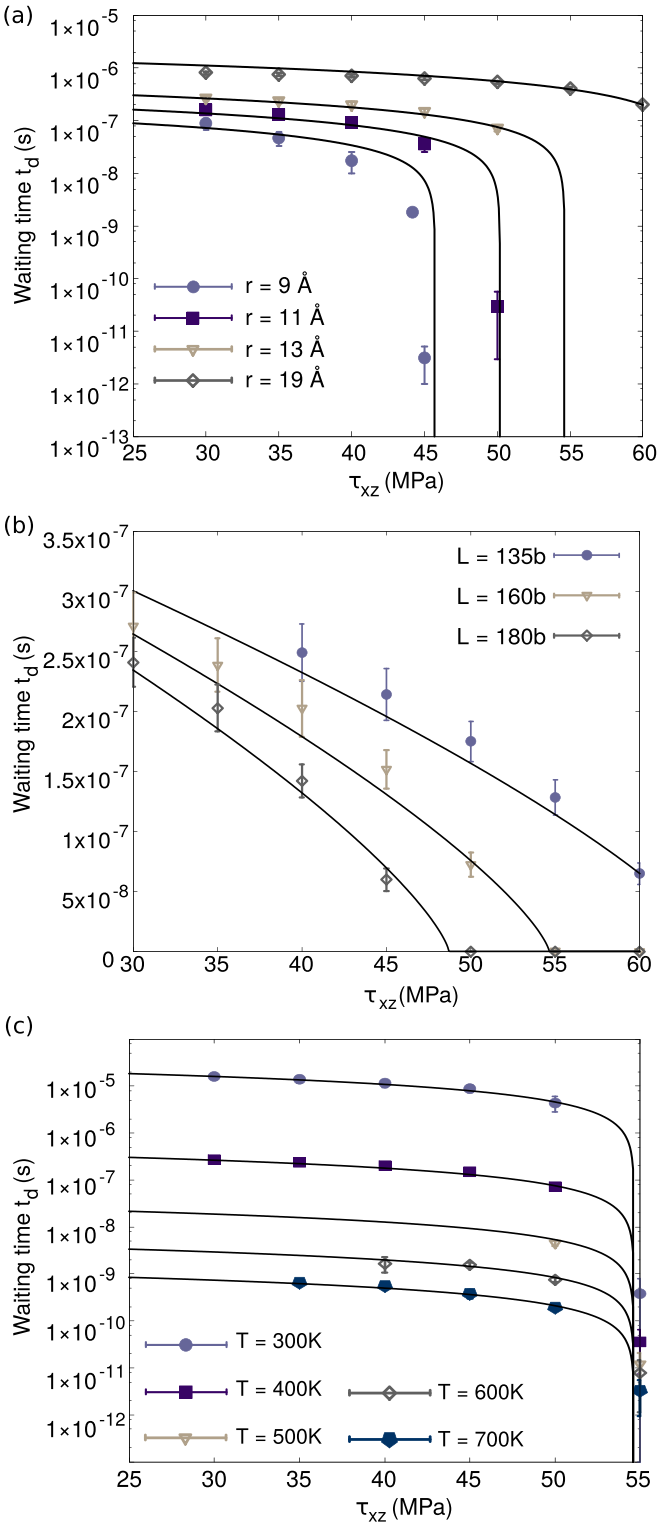

FIG. 15. (a) KMC-ELM simulations for the waiting time t_D of a dislocation anchored by a cluster of radius r against the applied shear stress τ_{xz}, for different r (see legend), at $T = 400$ K and a dislocation length $L = 160\ b$. (b) same as in (a) but for several dislocation line length L (see legend) and for $r = 13$ Å. (c) same as in (a) but for several temperatures T (see legend) and for $L = 160\ b$ and $r = 13$ Å. We have fitted the KMC-ELM simulation results (symbols) with Eq. (34) (lines).

expression:

$$t_D = \nu^{-1} h(r) g(T) \left(\frac{\tau_c - \tau_{xz}}{\tau_c} \right)^{3/4}, \tag{34}$$

where ν corresponds to the Debye frequency given in Eq. (28). The factor $h(r)$ intends to supplement the variation of t_D against the void radius r also present in τ_c:

$$h(r) = \left(\frac{r}{b} \right)^{a_1} \exp\left(a_2 \left(\frac{r}{b} \right) \right). \tag{35}$$

The contribution of thermal activation is approximated through the factor

$$g(T) = a_3 \exp\left(\frac{-a_5 + a_4 \ln T}{k_B T} \right). \tag{36}$$

A good agreement was obtained between the fit and our simulation data with $a_1 = 1.55$, $a_2 = 0.37$, $a_3 = 7 \times 10^{-3}$ s, $a_4 = 119.8$ meV, and $a_5 = 155.3$ meV. At high stress the results show a very sharp decrease of t_D. It is clearly visible for the smallest clusters: $r = 9 - 10$ Å in Fig. 15(a). Such a drop is explained by the fact that when the applied stress τ_{xz} approaches the critical stress τ_c, the unpinning occurs through dislocation glide with no need for activation of diffusion vacancy. In this case the dislocation unpinning is extremely fast and the diffusion no longer plays any significant role. Using Eq. (34) we reproduced the pinning time variation with stress. When $\tau_{xz} \geqslant \tau_c$ the pinning is inefficient and the dislocation glides freely. In such a case, t_D was fixed to zero. The temperature dependence has the form of an Arrhenius law in Eq. (36) with an energy barrier of $a5 = 155.3$ meV, close to the energy barrier for the vacancy emission (see Fig. 2). As for void shrinkage in Eq. (32), to obtain a good agreement with simulation results we had to introduce an effective variation of the Arrhenius energy barrier which decreases when the temperature increases. We have not found physical interpretations for such temperature variations of the effective barriers but we believe that this property deserves to be treated independently in a future study. For the purpose of the present study, we only needed an analytical form as given in Eq. (34).

In case of dislocation unpinning through simple glide the waiting time can write as follows:

$$t_d^{pg} \simeq \nu^{-1} \exp\left(\frac{\Delta H_{\text{act}}}{k_B T} \right). \tag{37}$$

In Fig. 16 we compared the waiting time computed from KMC-ELM model, in which the diffusion is taken into account, to the waiting time t_d^{pg}, determined through Eq. (37), in which the diffusion is neglected. We show clearly that at low stresses, the waiting time t_d^{pg}, neglecting the diffusion mechanisms, is much larger than KMC-ELM results. Therefore the diffusion plays a crucial role that accelerates the unpinning. However, when the shear stress approaches the critical stress, the diffusion becomes less and less important.

IV. MODELING KINETIC PROCESSES FOR A DISTRIBUTION OF CLUSTERS

In order to perform more realistic simulations, we have constructed three-dimensional random distributions of clusters with concentration and sizes typical from what was

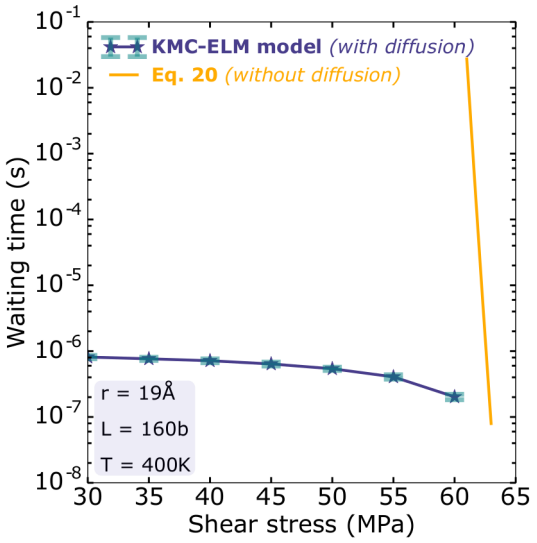

FIG. 16. Comparison between the waiting time computed with the KMC-ELM model and Eq. (37), for which the diffusion is neglected. We fixed the cluster radius r at 19 Å, the temperature T at 400 K and the dislocation line length L at 160b.

observed in experiments by Dai and Victoria in Cu after deformation [5] (see Fig. 17). The cluster concentration was fixed to 6.9×10^{22} m^{-3} and the average cluster radius was set to 25 Å. We did not find in the literature similar measurements for a single crystal of Al but we assumed that it is same order since the emergence of voids is related to the deformation of the fcc crystal with similar density of mobile dislocations.

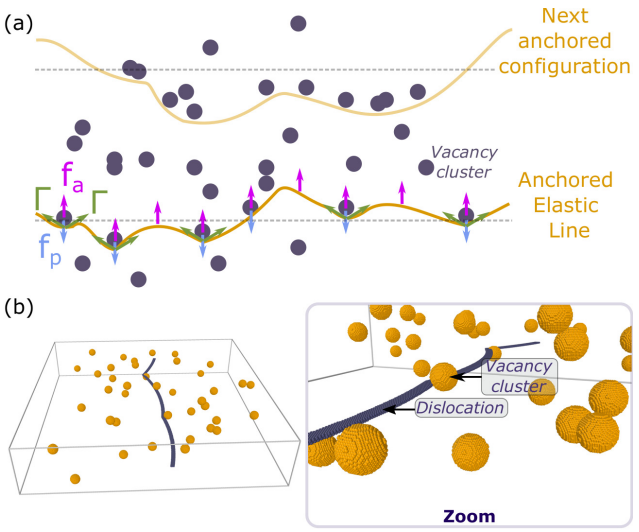

FIG. 17. (a) Schematic representation of two successive anchored configurations for the dislocation in interaction with a random distribution of vacancy clusters. (b) One anchored configuration in a small simulation cell of 500b × 500b × 500b. The concentration of clusters is 6.9×10^{22}m^{-3} and the cluster radius is $r = 25$ Å, the temperature is $T = 300$ K and the applied shear stress is $\tau_{xz} = 25$ MPa.

The elastic line must be several microns long to represent dislocations in real materials, and it must glide over distances of same order. With such dimensions the number of vacancies that needs to be introduced in our simulation is very large. As the dimensions of the simulation cell increase, it becomes extremely time consuming to treat the motion of each vacancy. In order to avoid an useless computational load we have treated each cluster as an obstacle, the pinning strength of which decreases with time as soon as the cluster is in contact with the dislocation. This trick allows us to reproduce the shrinkage of clusters through vacancy pipe diffusion, avoiding treating the motion of each vacancy individually. The criterion for the contact between the obstacle and the elastic line is defined by a distance inferior to the sum $(r + d_{ed}/2)$, where one recognizes the cluster radius and the dissociation distance d_{ed} [see Fig. 12(b)]. Using the function t_D in Eq. (34), the average waiting time of the dislocation can be determined for each cluster situated along the line. These clusters are characterized through only two parameters: (i) their radius r which allows us to determine the maximum pinning force f_p through Eq. (5) and (ii) the applied force exerted on the line segment l in interaction with the cluster

$$f_a = \tau_{xz} b u_y + \Gamma(x_{l+1} + x_{l-1} - 2x_l)/u_y, \tag{38}$$

which is computed at each step in our simulation. In order to compute the corresponding waiting time t_w we simply remarked that when the clusters are regularly spaced along the dislocation line, separated by a distance L then the balance of force along the line leads to $f_a = \tau_{xz} bL$ meanwhile $f_p = \tau_c bL$. Introducing such expressions in Eq. (34) we could evaluate the average waiting time for each obstacle:

$$t_w = \nu^{-1} h(r) g(T) \left(\frac{f_p - f_a}{f_p} \right)^{3/4}. \tag{39}$$

In the course of simulations, we have selected along the anchored elastic line, the obstacle that corresponds to the shortest waiting time $t_{\min}$. The pinning force f_p of that cluster is set to zero to force the crossing in the procedure of force relaxation and we incremented the simulation time by the corresponding $t_{\min}$. The pinning strength is updated for each cluster in contact with the elastic line since the radius of these clusters decrease with time (see Eq. (33) and Fig. 14).

The dimension of the simulation cell was fixed to $1000b$ in the direction of the dislocation line, $4000b$ in the glide direction, and $100b$ in the direction perpendicular to the climb plane. In Fig. 18 we have reported our simulation results for the average velocity of dislocation against the applied shear stress at various temperatures. The error bars are the standard deviations obtained through a sampling with 50 clusters distributions. We did not observe any significant variations with different dislocation lengths, i.e., $800b$ or $1200b$ (see green square and purple dot in Fig. 18). In their experimental study performed at 300 K and for a deformation rate of $\dot{\gamma} = 1.6 \times 10^{-6}$ s^{-1}, Jobba *et al.* [36] obtained a true stress of 10 MPa for ultrapure Al. We noticed that Dai and Victoria [5] estimated a comparable stress level of 16 MPa due to clusters in their sample containing a density of cluster of 6.9×10^{22} m^{-3}, i.e., the value used in our simulations. In the

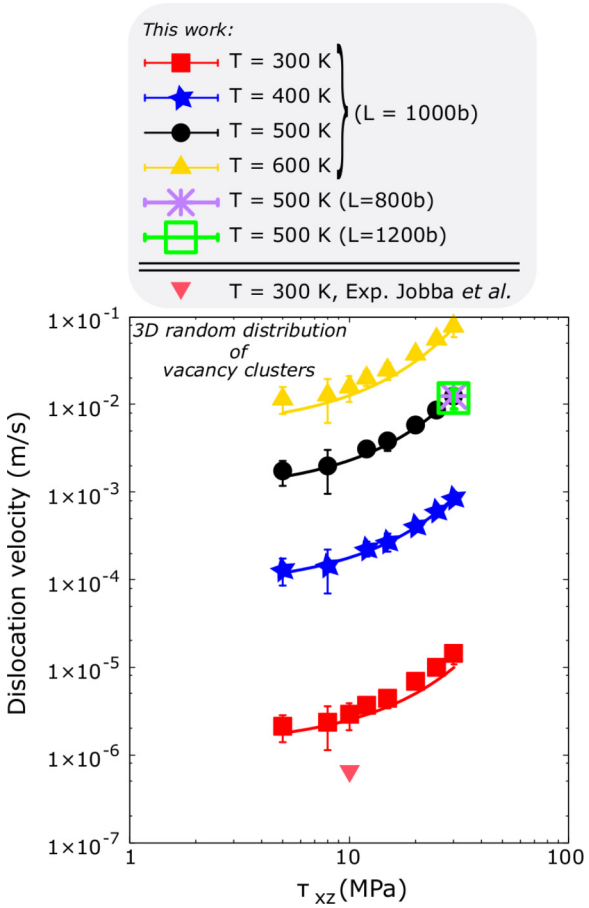

FIG. 18. Average velocity of a dislocation crossing random vacancy cluster distributions. We fixed the concentration for clusters to 6.9×10^{22} m^{-3} and the cluster radius to $r = 25$ Å. Simulations results (symbols) were reported against the applied shear stress τ_{xz} for several temperatures. The dislocation length was fixed to $1000b$, but we do not observe any significant variation of the velocity with a length fixed to $800b$ or $1200b$ (see legend). Averages and standard deviations were computed from sampling 50 random distributions.

well annealed sample of Al used in the experiments performed by Jobba *et al.* we can assume that the density of mobile dislocation is of the order of $\rho_d = 10^{12}$ m^{-2}. The use of the Orowan equation [75] $\dot{\gamma} = \rho_d b V_d$, where V_d stands for the average dislocation velocity, allows us to deduce that in the deformation tests performed by Jobba *et al.* the dislocation moves at a velocity of 0.56 10^{-6} m s^{-1} which agrees rather well with our simulation results reported in Fig. 18. The comparison between our computations and the experimental deformation test in ultrapure Al allows us to show that the vacancy clusters might contribute in a significant manner to hardening of metals. However, we must admit that we do not have enough experimental data about the typical size and the density of clusters in Al, to compute with accuracy their contribution to dislocations impeding. A rigorous comparison with deformation test experiments requires also to consider other contributions as those from the dislocation forest as it was proposed earlier by Foreman and Makin [69]. It seems yet possible to incorporate those obstacles in our simulations

with less difficulties than for vacancy clusters as their pinning strengths are not time dependent.

V. CONCLUSIONS

Our atomic scale simulations, described in Sec. II allowed us to determine the energy barriers for the main mechanisms involved in the dislocation crossing nano-voids. In agreement with the experiments [12–15] we have demonstrated that the vacancies, essentially emitted from clusters migrate through the dislocation core via a propitious pipe diffusion. Dislocation jogs are far less favorable vacancy sources than cavities and they were confirmed to correspond to perfect vacancy sinks [28,60]. We showed that the most stable position for vacancies is situated at the Shockley partial dislocations in the absence of a cavity. However, when the dislocation is anchored by a cavity the vacancy most favorable position is situated at the interface between the cavity and the dislocation where jogs form and eventually expand through vacancy accumulation. When the jogs are formed the driving force for cavity dissolution was found to derive from the vacancy trapping by jogs, which allows an energy gain far more important than the cost corresponding to remove a vacancy from a cavity.

Using our atomic scale data we built the KMC-ELM model allowing us to work at larger time and space scales. An elastic line model, adapted to model dislocations was bridged with a lattice kinetic Monte Carlo algorithm to treat vacancy thermally activated jumps. We estimated the evolution of the waiting time of a dislocation anchored by a vacancy cluster according to the applied shear stress, the cluster size and the temperature. In agreement with experiments [12–14], our computations showed a remarkably large acceleration of the void shrinkage when a dislocation is in contact with the void. In a previous work [38], we neglected the vacancy pipe diffusion leaks from nanovoids. Unfortunately, this assumption was incorrect, which invalidates the predictions for the dislocation creep reported in Ref. [38].

In order to treat the motion of a dislocation in a random distribution of voids, as observed by Dai and Victoria [5], we introduced an elastic line model where the pinning forces of the clusters evolve in time when they are in contact with the dislocation line. Such simulations allowed us to avoid the KMC integration of thermally activated jumps of each vacancy, which proved overwhelming for our computational capacities. The ELM was parametrized in agreement to KMC-ELM results. We computed the evolution of the dislocation average velocity as a function of applied stress and temperature, for a cluster concentration of 6.9×10^{22} m^{-3} and a typical radius of 25 Å [5]. The dislocation velocity found in our simulation at 300 K is slightly above 10^{-6} m/s, which is comparable to what was measured for a true stress of 10 MPa in deformation tests of ultrapure Al [36]. This comparison confirms that our nested simulations have been successful since we were able to realize simulations at the scale of realistic experiments while all the simulation parameters were derived from the atomistic scale. Our results also confirm the role played by nanovoids in hardening materials. The same combining of simulations could be applied to treat various issues in materials physics [21,53,76–78]. Furthermore it could certainly be improved using more precise atomic scale computations, either with more complex interatomic potentials [79] or machine learning computations [80].

ACKNOWLEDGMENTS

We gratefully acknowledge N. Mousseau and his colleagues S. Elliassen, S. Mahmoud and S. Gelin for helping one of us, M.L. to use ART-*nouveau*. We also gratefully acknowledge E. Clouet for his helpful advice.

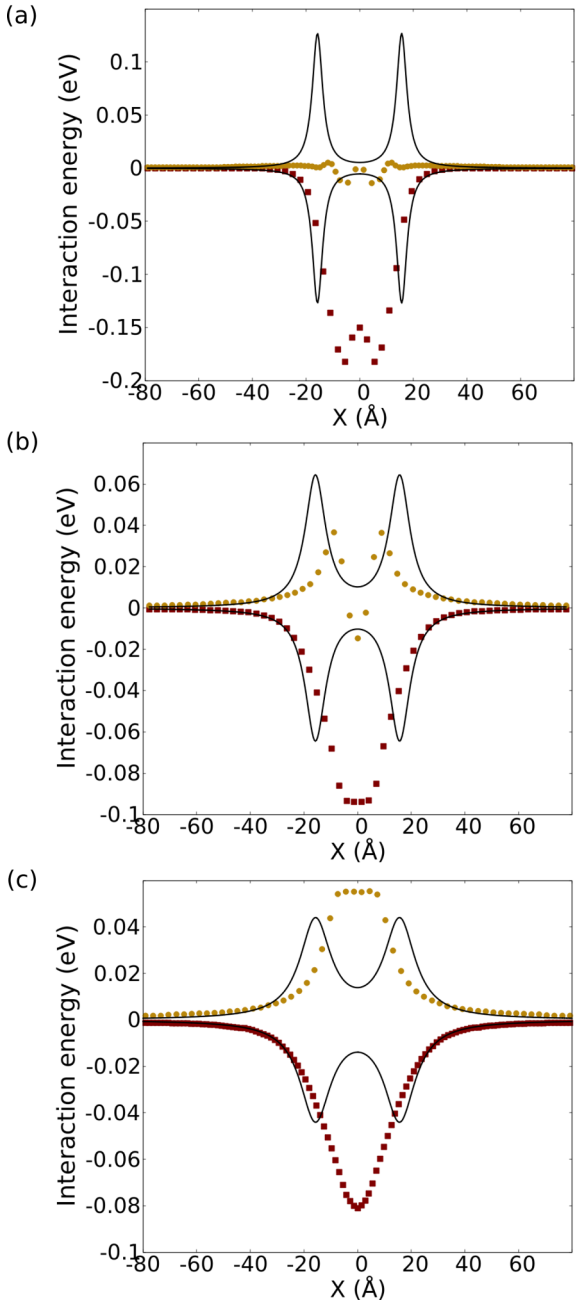

FIG. 19. Interaction energy, computed in MS, between a dislocation and a vacancy belonging to the n_Z plane above (red squares) or below (yellow dots) the dislocation glide plane. We compared the MS computations with the elasticity theory (black line) for (a) $|n_Z| = 1$, (b) $|n_Z| = 2$ or (c) $|n_Z| = 3$.

APPENDIX A: INTERACTION DISLOCATION/VACANCY: STATIC MOLECULAR COMPUTATIONS COMPARED TO ELASTICITY THEORY

Within the framework of the elasticity theory [54,81], the interaction energy between a dislocation and a vacancy can be written

$$E_{\text{int}}^{el} = \frac{\mu b}{6\pi}\frac{1+\nu}{1-\nu}\left(\frac{Z}{A_0}+\frac{Z}{B_0}\right)V_{\text{relax}},$$
$$A_0 = (X-d_{ed})^2+Z^2,$$
$$B_0 = (X+d_{ed})^2+Z^2, \quad \text{(A1)}$$

with the vacancy relaxation volume $V_{\text{relax}} = -6.6$ Å^3. X and Z are, respectively, the distance dislocation vacancy in $x[110]$ and in $z[1\bar{1}1]$ directions. A comparison between that theory and our atomic-scale simulations is plotted in Fig. 19 (see Sec. II C, for the simulation details). As it was noted by different authors [20,29] when the vacancy is situated in the vicinity of the dislocation core the elasticity theory does not describe the interaction energy. In main text, we used our atomic scale results to describe such interaction.

APPENDIX B: METHODOLOGY EMPLOYED TO DETERMINE THE MIGRATION BARRIERS FOR VACANCIES

We used the activation relaxation technique (ART-*nouveau*), that is a method to systematically search for saddle states in complex energetic landscapes [61,82–85]. ART-*nouveau* can also be used to find all the final states accessible from a given initial state. The only prerequisite is the initial state of the system, the other minima or saddle points are revealed by the method itself. Once ART-*nouveau* provided us final states we also used the NEB method [55–57] in order to refine our computation of the energy barrier between the initial and the final states.

In ART-*nouveau* a perturbation is applied to the initial state and the algorithm drives the system until a negative eigenvalue of the Hessian matrix is found [61,82–84]. We denote by $\mathbf{q}_{ini} \in \mathbb{R}^{3N_{\text{at}}}$ the initial state of the system, that is deformed iteratively. At the k^{th} step, the state of the system is given by

$$\mathbf{q}^k = \mathbf{q}^{k-1} + \frac{\delta x_A}{||\delta\mathbf{q}||}\delta\mathbf{q}\,, \quad \text{(B1)}$$

where δx_A is the amplitude of the perturbation applied between two images, fixed to 0.001 Å, while $\delta\mathbf{q}$ is the random direction of the initial deformation in the $\mathbb{R}^{3N_{\text{at}}}$ space. It was stated that local perturbation is numerically more efficient to reach saddle point convergence [85]. Consequently, in the present study, the initial perturbation is not applied on all the atoms, but is localized on the atoms in the vicinity of the defect. This proximity is defined within a cutoff radius of 2.5 Å [85] around the defect position.

For each step, a force relaxation is performed in the hyperplan perpendicular to δq^k and the 15$^{\text{th}}$ lower eigenvalues and eigenvectors of the Hessian matrix are determined using the Lanczos algorithm [85]. The size of the step for the numerical derivatives used in the Lanczos algorithm was fixed to 0.01 Å.

An inflection point is supposed to be reached, when the lowest eigenvalue of the Hessian is lower than a critical value, set to -1 eV/Å. In order to reach the saddle point, the perturbation after the inflection point is orientated following the direction opposite to the eigenvector, $\delta\mathbf{v}_m$, associated to the lowest eigenvalue [61,82–84]. The state of the system is then computed by

$$\mathbf{q}^k = \mathbf{q}^{k-1} - \frac{\delta x_C(k)}{||\delta\mathbf{v}_m||}\delta\mathbf{v}_m\,. \quad \text{(B2)}$$

Following the procedure developed by Cancès *et al.* [86], the amplitude of the perturbation applied between two images, $\delta x_C(k)$, is evaluated depending on the magnitude of the lowest eigenvalue, yielding a smooth convergence of the system toward the saddle point. The force criterion for the saddle-point convergence was fixed to 1.10^{-3} eV/Å. In order to concentrate our research on vacancy migration, we forbid events on the free surfaces of the simulation cell.

In the case of a vacancy near the dislocation core, we encountered some convergence problems with ART-*nouveau,* which had difficulties in obtaining the 12 possible barriers. For that reason, the ART-*nouveau* paths were refined with NEB calculations in the region defined by $-4 \leqslant n_Z \leqslant 4$. The NEB calculations were performed using five images and the force criterion was 5×10^{-4}eV/Å. The massive number of barrier calculations proved compulsory to build the input database for larger scale simulations.

[1] M. Kiritani, J. Nucl. Mater **276**, 41 (2000).
[2] S. Kojima, Y. Satoh, H. Taoka, I. Ishida, T. Yoshiie, and M. Kiritani, Philos. Mag. A **59**, 519 (1989).
[3] M. Loretto, L. Clarebrough, and R. Segall, Philos. Mag. **11**, 459 (1965).
[4] L. Clarebrough, P. Humble, and M. Loretto, Acta Metall. **15**, 1007 (1967).
[5] Y. Dai and M. Victoria, Acta Mater. **45**, 3495 (1997).
[6] S. Saimoto and B. Diak, Philos. Mag. **92**, 1890 (2012).
[7] S. Saimoto, B. Diak, and D. Lloyd, Philos. Mag. **92**, 1915 (2012).
[8] A. Chaudhuri, M. Singh, B. Diak, C. Cuoppolo, and A. Woll, Philos. Mag. **93**, 4392 (2013).
[9] M. Kiritani, Mater. Chem. Phys. **50**, 133 (1997).
[10] M. Kiritani, J. Nucl. Mater. **216**, 220 (1994).
[11] J. Crocombette, in *Handbook of Materials Modeling*, edited by S. Yip (Springer, Dordrecht, 2005).
[12] T. Volin and R. Balluffi, Appl. Phys. Lett. **11**, 259 (1967).
[13] T. Volin, K. Lie, and R. Balluffi, Acta Metall. **19**, 263 (1971).
[14] M. Legros, G. Dehm, E. Arzt, and T. Balk, Science **319**, 1646 (2008).
[15] H. Ogi, A. Tsujimoto, S. Nishimura, and M. Hirao, Acta Mater. **53**, 513 (2005).
[16] A. Sivak, V. Chernov, V. Romanov, and P. Sivak, J. Nucl. Mater. **417**, 1067 (2011).
[17] A. Vattré, T. Jourdan, H. Ding, M. Marinica, and M. Demkowicz, Nat. Commun. **7**, 10424 (2016).

[18] D. Carpentier, T. Jourdan, Y. Le Bouar, and M. Marinica, Acta Mater. **136**, 323 (2017).
[19] R. Fastenau and M. Baskes, Phys. Status Solidi A **75**, 323 (1983).
[20] E. Clouet, C. Varvenne, and T. Jourdan, Comput. Mater. Sci. **147**, 49 (2018).
[21] K. Baker and W. Curtin, J. Mech. Phys. Sol. **92**, 297 (2016).
[22] X. Zhang and G. Lu, Phys. Rev. B **82**, 012101 (2010).
[23] Q. F. Fang and R. Wang, Phys. Rev. B **62**, 9317 (2000).
[24] A. Ruoff and R. Balluffi, J. Appl. Phys. **34**, 1848 (1963).
[25] T. Volin and R. Balluffi, Phys. Status Solidi B **25**, 163 (1968).
[26] A. Bortz, M. Kalos, and J. Lebowitz, J. Comput. Phys. **17**, 10 (1975).
[27] L. Proville and S. Patinet, Phys. Rev. B **82**, 054115 (2010).
[28] D. Seidman and R. Balluffi, Phys. Status Solidi B **17**, 531 (1966).
[29] M. Kabir, T. T. Lau, D. Rodney, S. Yip, and K. J. Van Vliet, Phys. Rev. Lett. **105**, 095501 (2010).
[30] T. Swinburne, K. Arakawa, H. Mori, H. Yasuda, M. Isshiki, K. Mimura, M. Uchikoshi, and S. Dudarev, Sci. Rep. **6**, 30596 (2016).
[31] S. Hayakawa, T. Okita, M. Itakura, M. Aichi, and K. Suzuki, Philos. Mag. **98**, 2311 (2018).
[32] T. Okita, S. Hayakawa, M. Itakura, M. Aichi, S. Fujita, and K. Suzuki, Acta Mater. **118**, 342 (2016).
[33] Y. Gao, Z. Zhuang, Z. Liu, X. You, X. Zhao, and Z. Zhang, Int. J. Plast. **27**, 1055 (2011).
[34] C. Ayas, J. Van Dommelen, and V. Deshpande, J. Mech. Phys. Sol. **62**, 113 (2014).
[35] P. Geslin, B. Appolaire, and A. Finel, Appl. Phys. **104**, 011903 (2014).
[36] M. Jobba, R. Mishra, and M. Niewczas, Int. J. Plast. **65**, 43 (2015).
[37] H. Asada, R. Horiuchi, H. Yoshinaga, and S. Nakamoto, Trans. Jpn. Inst. Met. **8**, 159 (1967).
[38] M. Landeiro Dos Reis, L. Proville, and M. Sauzay, Phys. Rev. Mater. **2**, 093604 (2018).
[39] X. Liu, P. Ohotnicky, J. Adams, C. Rohrer, and R. Hyland, Surf. Sci. **373**, 357 (1997).
[40] F. Ercolessi and J. Adams, EPL **26**, 583 (1994).
[41] J. Bandyopadhyay and K. Gupta, Cryogenics **18**, 54 (1978).
[42] R. Reed, Cryogenics **12**, 259 (1972).
[43] S. G. Srinivasan, X. Z. Liao, M. I. Baskes, R. J. McCabe, Y. H. Zhao, and Y. T. Zhu, Phys. Rev. Lett. **94**, 125502 (2005).
[44] W. Triftshäuser, Phys. Rev. B **12**, 4634 (1975).
[45] R. Balluffi and A. Granato, Dislocat. Solids **4**, 1 (1980).
[46] M. J. Fluss, L. C. Smedskjaer, M. K. Chason, D. G. Legnini, and R. W. Siegel, Phys. Rev. B **17**, 3444 (1978).
[47] A. Seeger, D. Wolf, and H. Mehrer, Phys. Status Solidi B **48**, 481 (1971).
[48] J. Bass, Philos. Mag. **15**, 717 (1967).
[49] P. Tzanetakis, J. Hillairet, and G. Revel, Phys. Status Solidi B **75**, 433 (1976).
[50] T. Schlick, *Molecular Modeling and Simulation: An Interdisciplinary Guide* (Springer Science & Business Media, Berlin, 2010), p. 479.
[51] C. Runge, Math. Ann. **46**, 167 (1895).
[52] W. Kutta, Z. Math. Phys. **46**, 435 (1901).
[53] M. Bahramyan, R. Taherzadeh Mousavian, and D. Brabazon, Mater. Sci. Eng. A **674**, 82 (2016).
[54] E. Clouet, Acta Mater. **54**, 3543 (2006).
[55] H. Jónsson, G. Mills, and K. Jacobsen, in *Classical and Quantum Dynamics in Condensed Phase Simulations* (World Scientific, Hong Kong, 1998), pp. 385–404.
[56] G. Henkelman and H. Jónsson, J. Chem. Phys. **113**, 9978 (2000).
[57] G. Henkelman, B. Uberuaga, and H. Jónsson, J. Chem. Phys. **113**, 9901 (2000).
[58] D. Bacon, Y. Osetsky, and D. Rodney, Dislocat. Solids **15**, 1 (2009).
[59] N. Thomson, Proc. Phys. Soc. B **66**, 481 (1953).
[60] J. Hirth and J. Lothe, *Theory of Dislocations* (Wiley, New York, 1982), p. 569.
[61] N. Mousseau, L. Béland, P. Brommer, J.-F. Joly, F. El-Mellouhi, E. Machado-Charry, M.-C. Marinica, and P. Pochet, J. Atom. Mol. Opt. Phys. **2012**, 1 (2012).
[62] Y. Osetsky and D. Bacon, J. Nucl. Mater. **323**, 268 (2003).
[63] T. Hatano, Phys. Rev. B **74**, 020102(R) (2006).
[64] L. Proville and B. Bako, Acta Mater. **58**, 5565 (2010).
[65] J. Dérès, L. Proville, and M. Marinica, Acta Mater. **99**, 99 (2015).
[66] D. Bacon, U. Kocks, and R. Scattergood, Philos. Mag. **28**, 1241 (1973).
[67] R. Scattergood and D. Bacon, Philos. Mag. **31**, 179 (1975).
[68] H. Frost and M. Ashby, *Deformation Mechanism Maps: The Plasticity and Creep of Metals and Ceramics* (Pergamon, Oxford, 1982).
[69] A. Foreman and M. Makin, Philos. Mag. **14**, 911 (1966).
[70] K. Hanson and J. Morris, J. Appl. Phys. **46**, 983 (1975).
[71] A. Landau, Phys. Status Solidi A **30**, 659 (1975).
[72] J. Hirth and J. Lothe, *Theory of Dislocations* (Wiley, New York, 1982), p. 555.
[73] L. Proville, L. Ventelon, and D. Rodney, Phys. Rev. B **87**, 144106 (2013).
[74] J. Hirth and J. Lothe, *Theory of Dislocations* (Wiley, New York, 1982), p. 156.
[75] E. Orowan, Proc. Phys. Soc. **52**, 8 (1940).
[76] D. Bacon and Y. Osetsky, JOM **59**, 40 (2007).
[77] Y. Zhao, L. Dezerald, M. Pozuelo, and J. Marian, Nat. Commun. **11**, 1227 (2020).
[78] C. McElfresh, Y. Cui, S. Dudarev, G. Po, and J. Marian, Int. J. Plast. 102848 (2020).
[79] X. W. Zhou, D. K. Ward, and M. E. Foster, New J. Chem. **42**, 5215 (2018).
[80] A. M. Goryaeva, J.-B. Maillet, and M.-C. Marinica, Comput. Mater. Sci. **166**, 200 (2019).
[81] R. Bullough and R. Newman, Rep. Prog. Phys. **33**, 101 (1970).
[82] N. Mousseau and G. T. Barkema, Phys. Rev. E **57**, 2419 (1998).
[83] N. Mousseau and G. T. Barkema, Phys. Rev. B **61**, 1898 (2000).
[84] R. Malek and N. Mousseau, Phys. Rev. E **62**, 7723 (2000).
[85] M.-C. Marinica, F. Willaime, and N. Mousseau, Phys. Rev. B **83**, 094119 (2011).
[86] E. Cances, F. Legoll, M. Marinica, K. Minoukadeh, and F. Willaime, J. Chem. Phys. **130**, 114711 (2009).